HHS Public Access

Author manuscript

Nat Cancer. Author manuscript; available in PMC 2024 June 13.

Published in final edited form as:

Nat Cancer. 2024 March ; 5(3): 433–447. doi:10.1038/s43018-023-00704-x.

Loss of *Pip4k2c* confers liver-metastatic organotropism through insulin-dependent PI3K-AKT pathway activation

Meri Rogava[1,2,3], **Tyler J. Aprati**[4,*], **Wei-Yu Chi**[5,6,7,*], **Johannes C. Melms**[1,2,3], **Clemens Hug**[8], **Stephanie H. Davis**[8,†], **Ethan M. Earlie**[5,6,7,9], **Charlie Chung**[10], **Sachin K. Deshmukh**[11], **Sharon Wu**[11], **George Sledge**[11], **Stephen Tang**[1,2,3], **Patricia Ho**[1,2,3], **Amit Dipak Amin**[1,2,3], **Lindsay Caprio**[1,2,3], **Carino Gurjao**[1,2,3,12], **Somnath Tagore**[1,2,12], **Bryan Ngo**[6], **Michael J. Lee**[13], **Giorgia Zanetti**[3], **Yiping Wang**[1,2,3,12], **Sean Chen**[1,2,3], **William Ge**[4], **Luiza Martins Nascentes Melo**[17], **Gabriele Allies**[17], **Jonas Rösler**[17], **Goeffrey T. Gibney**[14], **Oliver J. Schmitz**[15], **Megan Sykes**[3], **Rémi J. Creusot**[3], **Thomas Tüting**[16], **Dirk Schadendorf**[17], **Martin Röcken**[18], **Thomas K. Eigentler**[19], **Andrei Molotkov**[20], **Akiva Mintz**[20], **Samuel F. Bakhoum**[21,22], **Semir Beyaz**[10], **Lewis C. Cantley**[6], **Peter K. Sorger**[8], **Sven W. Meckelmann**[15], **Alpaslan Tasdogan**[17,$], **David Liu**[4,$], **Ashley M. Laughney**[5,6,7,$], **Benjamin Izar**[1,2,3,12,#]

[1]Department of Medicine, Division of Hematology/Oncology, Columbia University Irving Medical Center, New York, NY, USA

[2]Herbert Irving Comprehensive Cancer Center, Columbia University Vagelos School of Physicians and Surgeons, New York, NY, USA

[3]Columbia Center for Translational Immunology, Columbia University Irving Medical Center, New York, NY, USA

[4]Department of Medical Oncology, Dana-Farber Cancer Institute, Boston, MA, USA

[5]Department of Physiology, Biophysics, and Systems Biology, Weill Cornell Medicine, New York, NY, USA

[6]Meyer Cancer Center, Weill Cornell Medicine, New York, NY

[7]Institute for Computational Biomedicine, Weill Cornell Medicine, New York, NY, USA

[8]Laboratory for Systems Pharmacology, Harvard Medical School, Boston, MA, USA

[#]Corresponding author: bi2175@cumc.columbia.edu.
[$]these authors jointly co-supervised the work
[*]these authors contributed equally
[†]Deceased

Author contributions

B.I. conceived of and supervised the work. Me.Ro., designed, performed and analyzed all key experiments. J.C.M, S.H.D., C.C., S.Ta., P.H., A.D.A., L.C., M.J.L., G.Z., B.N. S.C., R.J.C. and O.S. performed and supported experiments. Me.Ro. and C.H. analyzed CRISPR screens and *in vitro* RNA-seq data. T.J.A., S.K.D., S.W., C.G., S.Tag., Y.W., W.G. and D.L. analyzed patient RNA-seq data newly generated here, assembled from publicly available data, or the Caris Life Sciences data. W-Y.C., E.M.E. and A.M.L. analyzed scRNA-seq data. L.M.N.M, G.A., J.R. S.W.M., A.T. generated and analyzed metabolomics data. A.Mo. and A.Mi. performed PET-CT imaging studies. G.S., G.T.G., T.T., D.S., Ma.Rö., T.K.E. and S.F.B. provided key materials, reagents or data. M.S., S.B., L.C.C., P.K.S., A.T., D.L. and A.M.L. provided additional study supervision. Me.Ro. and B.I. wrote the initial and revised manuscript with input and contributions from all authors. All authors approved of the revised manuscript.

Reporting summary

Further information on experimental design is available in the Nature Research Reporting Summary linked to this paper.

Code Availability

No custom algorithms were used in this study.

[9]Tri-Institutional Training Program in Computational Biology and Medicine, Weill Cornell Medicine, New York, NY 10065, USA

[10]Cold Spring Harbor Laboratory, Cold Spring Harbor, NY, USA.

[11]Caris Life Sciences, Phoenix, Arizona.

[12]Department of Systems Biology, Program for Mathematical Genomics, Columbia University, New York, NY, USA

[13]Department of Pathology and Cell Biology, Columbia University Irving Medical Center, New York, NY, USA

[14]Georgetown Lombardi Comprehensive Cancer Center, Washington, DC, USA.

[15]Applied Analytical Chemistry, University of Duisburg-Essen, Essen, Germany

[16]Laboratory for Experimental Dermatology, Department of Dermatology, University of Magdeburg, Magdeburg, Germany.

[17]Department for Dermatology, Venerology and Allergology, University Hospital Essen, NCT West, Campus Essen, German Cancer Consortium, Partner Site Essen & University Alliance Ruhr, Research Center One Health, Essen, Germany.

[18]Department of Dermatology, University Hospital Tuebingen, Tuebingen, Germany.

[19]Department of Dermatology, Venerology and Allergology, Charité University Hospital, Berlin, Germany

[20]Department of Radiology, Columbia University Medical Center, New York, NY, USA.

[21]Human Oncology and Pathogenesis Program, Memorial Sloan Kettering Cancer Center, New York, NY, USA.

[22]Department of Radiation Oncology, Memorial Sloan Kettering Cancer Center, New York, NY, USA.

Abstract

Liver metastasis (LM) confers poor survival and therapy resistance across cancer types, but the mechanisms of liver-metastatic organotropism remain unknown. Through *in vivo* CRISPR-Cas9 screens, we found that *Pip4k2c* loss conferred LM, but had no impact on lung metastasis or primary tumor growth. *Pip4k2c*-deficient cells were hypersensitized to insulin-mediated PI3K/AKT signaling and exploited the insulin-rich liver milieu for organ-specific metastasis. We observed concordant changes in *PIP4K2C* expression and distinct metabolic changes in 3,511 patient melanomas, including primary tumors, LMs and lung metastases. We found that systemic PI3K inhibition exacerbated LM burden in mice injected with *Pip4k2c*-deficient cancer cells through host-mediated increase in hepatic insulin levels, however, this circuit could be broken by concurrent administration of an SGLT2 inhibitor or feeding of a ketogenic diet. Thus, this work demonstrates a rare example of metastatic organotropism through co-optation of physiological metabolic cues, and proposes therapeutic avenues to counteract these mechanisms.

Introduction

Metastasis is a major determinant of mortality in patients with cancer[1], and metastatic patterns have important clinical and therapeutic implications[2]. Liver metastasis (LM) occurs frequently across different cancer types, including melanoma, and carcinomas of the colon, pancreas and breast[3] and confers a poor prognosis and reduced response rates to modern cancer therapies, such as immune checkpoint blockade (ICB), when compared to response rates in other common metastatic sites, such as the lung[3–5]. The underlying mechanisms for these clinical phenotypes are poorly understood. This is in part due to difficulties in modeling of salient molecular underpinnings of metastatic organotropism pre-clinically.

Despite extensive efforts in a variety of disease contexts, divergent somatic mutations that fully explain organ-specific metastasis have not yet been identified[6,7]. While this may be due to the limited power of individual studies and extensive disease heterogeneity, it is likely that other biological factors underly cancer organotropism. Indeed, recent work in melanoma patients, for example, revealed a higher rate of chromosomal instability, a neural-like cell state and metabolic adaptation enriched in the brain metastases compared to extra-cranial metastases[8]. Whether similar organ-specific mechanisms exist for other sites is unknown.

The liver is the major metabolic organ, where a multitude of cues are generated, received, and integrated, to regulate the supply of systemic nutrients, such as glucose and fatty acids[9]. Additionally, the liver has a dual blood supply via the hepatic artery and the portal vein, each of which may be a route for metastatic spread. There is also increasing evidence for hepatic modulation of local and peripheral immunity[10,11]. These and other distinct organ features may contribute to the liver-metastatic niche in melanoma, and other cancers.

To identify determinants of liver-metastatic organotropism in an unbiased fashion, we leveraged a syngeneic murine melanoma model, and performed large-scale CRISPR-Cas9 screens. We identified loss of *Pip4k2c* as driver of liver- but not extra-hepatic metastasis. We showed that this organotropism is due to co-optation of the insulin-rich liver milieu, to which *Pip4k2*-deficient cells are hypersensitized to, and unraveled downstream signaling, and metabolic and transcriptomic adaptations enriched in liver metastases in mouse and patient tumors. We observed a paradoxical increase in LM burden in animals treated with systemic PI3K inhibitors and showed that this was due to host-mediated responses that exacerbated the insulin-gradient, thereby promoting metastatic selectivity of *Pip4k2c*-deficient cells to the liver. Combination of PI3K inhibition with either systemic SGLT2 inhibition or feeding animals a ketogenic diet, reduced LM burden, while having little effect on other metastatic sites or primary tumor growth. Analyses and additional functional validation in prostate cancer and colorectal cancer models indicate a similar role of *Pip42kc* in conferring liver metastasis, suggesting that the proposed biological and therapeutic principles may extend beyond melanoma.

Results

CRISPR screens reveal determinants of liver metastasis

To identify drivers of liver metastasis, we used a syngeneic melanoma model, HCmel12, which was derived from *Hgf/Cdk4*^{R24C} mice that spontaneously develop melanoma[12] and recapitulates the potential for liver metastasis and therapeutic response patterns seen in patients with metastatic melanoma[13,14]. We performed a large-scale *in vivo* CRISPR-Cas9 screen in Cas9-expressing HCmel12 cells, perturbing 713 kinases in the mouse genome with 2,852 single-guide RNAs (sgRNAs) (four per target gene, and 100 non-targeting control guides using the "Brie" library[15]) (Fig. 1a, Extended Data Fig. 1a–c). The edited cell pool (Cas9 + Brie), as well as Cas9-expressing cells without sgRNAs and parental cells, were injected via tail vein or subcutaneously implanted in C57BL/6 (B6) animals. In parallel, edited cell lines were maintained *in vitro* and collected at several time points for the duration of the experiment (Methods). Dissection of animals (Methods) revealed that the Cas9 + Brie group had a significantly higher rate of animals with liver metastasis (Fig. 1b–d), higher metastasis count per animal (Fig. 1e), and increased liver metastatic burden compared to the Cas9 and parental groups (Fig. 1f), while there was no difference in lung metastatic burden across these groups (Fig. 1g). This suggested that loss of kinases targeted by the Brie sgRNA library enhanced the liver metastatic potential of HCmel12 melanoma cells.

Before identifying perturbations that may alter liver metastatic potential, we first assessed the sgRNA library complexity within the plasmid pool, edited cells, transplanted primary tumors, and distant metastasis (liver, lung and lymph nodes). Compared to the plasmid pool, cell line input, and primary tumors, which showed preserved and co-correlated library diversity, sgRNA diversity decreased substantially in metastatic lesions (Extended Data Fig. 1d–e) across different sites, while samples from the same metastatic sites showed stronger co-correlation (Extended Data Fig. 1d). In line with this, principal component analysis (PCA) of sgRNA representations revealed clades of metastases and transplanted tumors/cell lines along the PC1 (explaining 49.7% of variability) and PC2 (5.4 % of variability) (Extended Data Fig. 1f). Next, we identified sgRNAs targeting essential genes (e.g., *Plk1*, *Cdk7* and *Cdk12*) that were depleted after 14 days of editing in cells prior to injection into animals (Extended Data Fig. 2a–c, Supplementary Table 1). Additionally, sgRNAs targeting *Cdk4*, a known dependency in HCmel12, were also significantly depleted (log2FC=-10.206, FDR<0.06). Compared to edited cells prior to injection, primary tumors showed significant depletion of multiple genes, including *Jak1* and *Jak2*, suggesting that the Jak/Stat pathway may be important for tumor growth, as absence of intact *Jak1/Jak2* has been implicated in immune evasion[16]. *Stk11* was also depleted in primary tumors; loss of *Stk11* (encoding for Lkb1) promotes metastasis and confers therapy resistance[17]. The most strongly enriched perturbation involved in primary tumor growth was loss of *Dapk3* (log2FC=4.3693, FDR<0.007) (Extended Data Fig. 2b, Supplementary Table 2), a putative tumor suppressor gene whose deleterious mutations or loss occurs in up to ~7% of melanomas[18]. Together, these data suggested that the conducted screen was robust and yielded known and unknown biology, with sgRNA diversity reducing along the metastatic progression axis. This observation suggested that a small fraction of perturbations may determine metastatic potential[19].

We next sought to identify sgRNAs associated with metastatic potential to the liver. We used three criteria to nominate such putative drivers: sgRNAs that **(1)** are enriched with an FDR <0.1 and/or **(2)** account for >2% of sequencing reads within a given lesion and/or **(3)** are enriched in two or more biological replicates. We identified 80 sgRNAs that meet one (65), two (17) or all (2) of these criteria (Supplementary Table 3). Among the genes targeted by these sgRNAs are those involved in cell motility (*Tesk1, Pkn1, Mylk4*)[20–22], nucleotide homeostasis and metabolism (*Prps1, Prps2, Adck2, Nme8*)[23], modulation of insulin sensing (*Trib1, Pip4k2c*)[24–26], or function as tumor suppressors (*Fgfr3*)[27], such that the loss of these genes would promote hallmarks of metastasis. The "top hit" in this screen by all applied metrics was loss of *Pip4k2c* which encodes Phosphatidylinositol-5-Phosphate 4-Kinase Type 2 Gamma. Specifically, loss of *Pip4k2c* was the most enriched perturbation in five of 14 (~36%) investigated liver metastatic lesions. In all of these lesions, sgRNAs targeting *Pip4k2c* accounted for the majority of sequencing reads, while in four of these five lesions, this perturbation accounted for >98% of sequencing reads (Fig. 1h,i, Extended Data Fig. 2d). Furthermore, loss of *Pip4k2c* was the only perturbation (at an FDR <0.06), that was highly specific to liver metastasis (Extended Data Fig. 2e). These findings suggest that *Pip4k2c* loss may uniquely promote liver metastasis.

Pip4k2c loss sensitizes cells to insulin-mediated signaling

Pip4k2c is part of the Pip4k family that consists of three isoforms in both mice and humans[24]. The role of these kinases is poorly understood, but recent work suggests that Pip4k's, and the gene product of *Pip4k2c*, suppress Pip5k activity in response to insulin. This results in reduced production of phosphatidylinositol-4–5-bisphosphate (PI (4,5) P_2), the substrate of PI3 Kinase (PI3K), which converts PI (4,5) P_2 to phosphatidylinositol-3-4-5-triphosphate (PI (3,4,5) P_3) to subsequently activate AKT. Thus, we hypothesized that loss of *Pip4k2c* would lead to hyperactivation of the PI3K/AKT pathway in response to insulin. We hypothesized that because the liver is the organ with the highest insulin concentration (outside of the pancreas, where it is produced), *Pip4k2c*-loss mediated PI3K/AKT hypersensitization to insulin in tumor cells could encourage formation of an organ-specific metastatic niche.

To test whether *Pip4k2c* promotes PI3K/AKT hypersensitivity to insulin in melanoma cells, we generated HCmel12-*Pip4k2c*-KO cell lines ($Pip4k2c^{KO}$) using four different sgRNAs, including the top enriched sgRNA in our *in vivo* screen (Extended Data Fig. 3a–b). We next determined the impact of $Pip4k2c^{KO}$ on downstream PI3K/AKT pathway activation in response to insulin. Compared to parental cells, insulin stimulation of $Pip4k2c^{KO}$ resulted in higher and prolonged induction of phosphorylated AKT in both murine HCmel12 and the human melanoma model A375 (Fig. 2a,b, Extended Data Fig. 3c–e), increased phosphorylation of insulin receptor (INSR) (Extended Data Fig. 3f) and showed increased cell migration capacity, while the proliferation rate was not altered (Extended Data Fig. 3g–j). Bulk RNA-sequencing of parental compared to $Pip4k2c^{KO}$ cells stimulated with insulin revealed enrichment of mTOR pathway activity (Extended Date Fig. 3k, Supplementary Table 4). We rescued $Pip4k2c^{KO}$ with one of two open reading frames (ORFs): full-length ($Pip4k2c^{Rec}$) or allosteric-domain deficient (aa69–75 (VMLLPDD → EIFLPNN)) ($Pip4k2c^{AD}$), which was previously implicated in Pip4k2c

function[24] (Extended Data Fig. 3l–n). While *Pip4k2c*^{AD} continued to demonstrate high baseline and insulin-mediated Akt phosphorylation, *Pip4k2c*^{Rec} had lower p-Akt levels in both human and murine melanoma models (Extended Data Fig. 3l–n). This suggests that lack of the allosteric domain, but not the kinase domain of *Pip4k2c*, is sufficient to confer hypersensitization to insulin; this finding is consistent with prior work showing that *Pip4k2c* has very poor kinase activity[24]. Treatment with pan-PI3K inhibitor GDC-0941 (pictilisib) (with and without insulin stimulation) (Extended Data Fig. 3l–n) completely abrogated baseline Akt phosphorylation in cells with all of these genotypes, while insulin partly rescued PI3K activity (Extended Data Fig. 3l–n), which is consistent with a prior report[28]. We also tested PI3K alpha inhibitor BYL-719, which overall showed lower efficacy but similar results for insulin-mediated bypass activation (Extended Data Fig. 3l–n).

Loss of *Pip4k2c* confers liver-metastatic organotropism

To validate the role of *Pip4k2c* loss *in vivo*, we next injected either parental (*Pip4k2c*^{WT}), *Pip4k2c*^{KO}, *Pip4k2c*^{Rec}, or *Pip4k2c*^{AD} HCmel12 melanoma cells via tail vein in B6 mice. *Pip4k2c*^{KO} resulted in a significantly increased LM burden that was rescued by *Pip4k2c*^{Rec}, but not *Pip4k2c*^{AD} (Fig. 2c). Importantly, none of these perturbations altered lung metastatic burden (Fig. 2d). Consistently, loss of *PIP4K2C* in human melanoma cell line A375 conferred significantly increased metastasis to the liver, but not to the lung (Fig. 2e,f, Extended Data Fig. 3o). To determine whether *Pip4k2c* loss plays a role in LM development in other cancers that also frequently metastasize to the liver, we generated *Pip4k2c* KO in a colorectal cancer cell line (CT26) and orthotopically implanted these or parental cells into the colonic submucosa of BALB/c mice. Primary tumors arising from parental CT26 resulted in LM in 20% while *Pip4k2c*^{KO} cells gave rise to LM in 75% of animals (Fig. 2g). Notably, *Pip4k2c*^{KO} gave rise to smaller primary colorectal tumors (Fig. 2h), thus, indicating that higher rates of LM development were due to increased invasive capacity, as observed in melanoma models (Fig. 2c,e). Together, these results suggest that loss of *Pip4k2c* hypersensitizes cancer cells to insulin mediated PI3K/AKT hyperactivation, and thereby mediates metastasis specifically to the liver, but not to the lung.

Systemic PI3K inhibition enhances LM through host effects.

Since PI3K-i could abrogate PI3K/AKT signaling *in vitro* (Extended Data Fig. 3m–n), we reasoned that systemic treatment with the same drug would reduce LM burden *in vivo*. We injected parental or *Pip4k2c*^{KO} cells and treated animals with either vehicle control or GDC-0941 (Methods). Surprisingly, we found that liver-metastatic burden was significantly *increased* in animals bearing *Pip4k2c*^{KO} tumor cells, while lung metastatic burden was not altered (Fig. 3a,b). We reasoned that this paradoxical increase in LM burden in *Pip4k2c*^{KO} tumor bearing mice in response to PI3K inhibition may be explained by the effects of the drug on the host, which may promote liver metastasis in an insulin-dependent manner. Indeed, treatment with GDC-0941 resulted in a significant increase in blood glucose levels that peaked at 60 minutes after administration and was sustained for at least 90 minutes (Fig. 3c). Accordingly, the levels of C-peptide, a short amino-acid polypeptide of pro-insulin and equimolar surrogate for insulin production, were significantly increased in GDC-0941 treated animals with either *Pip4k2c*^{WT} or *Pip4k2c*^{KO} bearing tumors (Fig. 3d, Extended Data Fig. 3p), suggesting that these differences in metastatic burden

are explained by host responses to this treatment. To assess whether GDC-0941 induced glucose and insulin spikes influenced metastatic tumor cell sensitivity to insulin *in situ*, we treated *Pip4k2c*^{KO} liver-metastasis bearing mice with GDC-0941 or vehicle control. After 60 minutes when blood glucose concentration peaks following PI3K-i treatment, we performed [F18] fluorodeoxyglucose micro positron-emission tomography (FDG μPET). We found that *Pip4k2c*^{KO} liver metastases had a 3-fold increase in FDG uptake in PI3K-i treated mice (Fig. 3e, f). Lastly, we directly measured homeostatic levels of insulin in livers and lungs, confirming significantly higher levels in the hepatic environment (Fig. 3g). If high insulin concentration in the liver is an important cue for liver-metastatic organotropism, we reasoned that increasing insulin levels in the lung should increase the rate of metastasis to this organ. To test this, we subcutaneously implanted mice with slow-release insulin pads (Fig. 3h), which continuously deliver high systemic levels of insulin, followed by injection of cancer cells via tail vein, and determined liver and lung metastatic burden. While insulin delivery resulted increased metastatic burden was increased in both liver and lung (Fig. 3i), there was a significantly elevated lung-metastatic potential compared to control pad-implanted animals (Fig. 3j, k), suggesting that some disease burden was diverted to the lungs with higher local insulin levels. Together, these results suggest that *Pip4k2c*^{KO} cells efficiently co-opt the insulin-rich liver milieu for metastasis, and this can be further enhanced by host responses to PI3K inhibition.

Human and murine LM exhibit distinct metabolic adaptations

To further examine cancer cell states in liver compared to lung metastases, we performed single-cell RNA-sequencing (scRNA-seq) of eight mice with concurrent liver and lung metastases. Following rigorous quality control (Methods, Supplementary Tables 4 and 5), a total of 95,606 cell transcriptomes were included for downstream analyses. We identified tumor cells by their expression of melanocytic lineage markers, including *Mitf*, *Mlana*, *Dct*, *Tyr*, and *Tyrp1*. Differential gene expression and subsequent GSEA of melanoma cells revealed strong enrichment of metabolic pathways in cells isolated from liver metastases, including regulation of oxidative phosphorylation (Fig. 4a, Extended Data Fig. 4a–g). In support of the observations in melanoma, we analyzed another bulk RNA-seq data set of a prostate cancer model[29] that develops metastasis to multiple organs, including to liver, lung, and bone, and find the same metabolic pathway enrichment in liver compared to lung metastases (Fig. 4b).

To determine the relevance of these phenotypic differences in a patient context, we performed RNA-sequencing of melanoma LMs and combined these with publicly available data (Methods)[30], totaling 252 metastasis transcriptomes, including 93 liver metastases (Supplementary Tables 4 and 5). Comparison of LM transcriptomes with lung metastases revealed strong enrichment of metabolic pathways in LM, including TCA cycle, OxPhos, and mTORC1 signaling (Fig. 4c, Extended Data Fig. 4 h–j**, and** Supplementary Tables 4 and 5). These results were maintained when including only samples with high purity, reducing potential transcriptome contamination by healthy hepatocytes (Extended Data Fig. 4j,k, Supplementary Tables 4 and 5). Additionally, our scRNA-seq pathway analyses were exclusively performed on tumor cells yielded comparable results. To comprehensively determine the role of these observations in a large real-world data set, we analyzed 3,511

cutaneous melanoma patients, including 2404 primary cutaneous melanomas (PCMs), 364 LMs and 743 lung metastases (Supplementary Table 4). For all specimens, tumor regions were enriched through macro-dissecting and profiled using RNA-sequencing and exome sequencing (either whole-exome or 592 gene panel DNA-sequencing) at Caris Life Sciences (Phoenix, AZ). We found strong enrichment of metabolic pathways, including TCA cycle and OxPhos in LMs compared to PCMs and lung metastases (Fig. 4d), which mirrored our observations in mouse models (Fig. 4a,b) and publicly available patient data analyzed here (Fig. 4c). Overall, these transcriptomics data suggest that cancer cells in the liver enrich for key metabolic pathways when compared to other metastatic sites, both in melanoma and other cancers. In the same patient cohort, we found that *PIP4K2C*, but *PIP4K2A* or *PIP4K2B*, had a lower expression in LMs compared to PCMs and lung metastases ($p<0.0001$ and $p=0.08$, respectively) (Fig. 4e, f. Extended Data Fig. 4l. m). Additionally, comparison of genomics of LMs with either PCM or lung metastases in these patients showed distinct distribution of common oncogenic driver mutations, including *BRAF*, *NRAS* and *NF1*, and revealed an enrichment of the less commonly mutated (in melanoma) gene *PIK3CA* encoding for p110α, the catalytic subunit of PI3-kinase in LMs compared to PCMs and lung metastases (4.27% vs. 1.21%, $p=0.003$, and 4.27% vs. 2.34%, $p=0.19$, respectively) (Extended Data Figure 4n). Similarly, we found lower expression of *Pip4k2c*, but not *Pip4k2a/b*, in LMs compared to other metastatic sites in the Arriaga et al., prostate cancer metastatic mouse model data (Fig. 4g, Extended Data Fig. 4o).

We next sought to directly measure potential differences in metabolites between liver and lung metastases. For this purpose, we injected A375 cells (parental or $Pip4k2c^{KO}$) and collected liver and lung metastases (Methods). We performed mass spectrometry on five liver and five concurrent lung metastases from animals injected with $Pip4k2c^{KO}$ cells, and three liver and five lung metastases from mice injected with $Pip4k2c^{WT}$ cells. Principal component analysis (PCA) demonstrated that across and within each genotype, disease site (liver vs. lung) was the most important driver of variability in metabolic profiles (Extended Data Fig. 5a,b, Supplementary Table 6). Several key metabolites of the TCA cycle, including a-ketoglutarate, succinate, fumarate and malate were found at higher abundances in liver compared to lung metastases (Figure 4h, Extended Data Fig. 5c–e), consistent with the findings indicated from our transcriptomics analyses (Figure 4a–d).

INSR is necessary for liver-metastatic organotropism

Our data suggest that co-optation and metabolic adaptions to the insulin-rich liver milieu are strongly associated with liver-metastatic organotropism. To determine whether insulin acting on cancer cells is necessary for both liver-metastatic organotropism and increased disease burden in response to systemic PI3K inhibition, we transduced parental or $Pip4k2c^{KO}$ cells with a doxycycline(dox)-inducible short hairpin RNA (shRNA) targeting the insulin receptor (*Insr*) to generate otherwise isogenic, conditional *Insr* knockdown ($Insr^{shIR}$) or $Pip4k2c^{KO}/Insr^{shIR}$ cells (Fig. 5a). As expected, we found a significantly impaired induction of Akt phosphorylation in response to insulin in both dox-induced $Insr^{KD}$ and $Pip4k2c^{KO}/Insr^{shIR}$ cells, compared to their non-dox treated counterparts. Across all conditions, GDC-0941 effectively abrogated p-AKT (Extended Data Fig. 6a). Next, we injected mice with dox-treated or untreated $Pip4k2c^{KO}/Insr^{shIR}$ tumor cells followed by treatment with vehicle

or GDC-0941. *Insr* knockdown alone resulted in LM reduction compared to non-Dox treated animals (albeit not statistically significant), and in mice treated with GDC-0941, *Insr* knockdown in *Pip4k2c*^{KO} tumor cells resulted in a significantly reduced LM burden (Fig. 5b). Across all conditions, there was no change in lung metastasis burden (Fig 5c). Overall, these results suggest that while GDC-0941 effectively abrogates Akt phosphorylation *in vitro*, host responses to the drug and subsequent insulin-dependent circuitry increase metastasis to the liver, but not in the lung.

Combination interventions reduce LM burden

We reasoned that abolishing the PI3K-i-induced forward loop could reduce liver metastatic burden. To test this, we treated animals with an inhibitor of sodium-glucose co-transporter 2 (SGLT2i), that inhibits glucose re-uptake in the kidney, thereby, preventing spikes in insulin levels, or we fed animals a ketogenic diet that depletes glycogen storage (**Methods**). Peak blood glucose and plasma C-peptide levels were strongly reduced when combining GDC-0941 with SGLT2i or a ketogenic diet (Fig. 5d,e). In *Pip4k2c*^{KO} LM-bearing animals, combination of either SGLT2i or a ketogenic diet with GDC-0941 significantly reduced liver metastasis compared to animals receiving GDC-0941 alone (Fig. 5f). Notably, combination of ketogenic diet with GDC-0941 also significantly reduced lung metastatic burden, while SGLT2i plus GDC-0941 selectively targeted liver-metastatic disease (Fig. 5g), suggesting that addition of SGLT2i and a ketogenic diet to PI3K-i could circumvent GDC-0941-induced increase in LM. Importantly, compared to parental cells, loss of *Pip4k2c* had no differential impact on growth of subcutaneously implanted tumors or responses to GDC-0941 or GDC-0941 plus SGLT2i (Fig. 5h,I, Extended Data Fig. 6b). This is consistent with the initial CRISPR-Cas9 screen and suggests PI3Ki-based therapeutic combinations are critical for abrogating insulin-mediated circuits that are most pronounced in LM (Fig. 6).

Discussion

Not all metastatic sites are created equal. Compared to other sites, metastasis to the liver confers a poorer prognosis across multiple cancer types and reduced responses to modern cancer therapies[4,31,32]. Mechanisms that determine a cancer cell's metastatic fate towards one organ site over another are poorly understood and are not sufficiently accounted for by a model of serial, divergent acquisition of somatic mutations[33,34]. The fact that cancer types with different oncogenic dependencies and distinct lineages exhibit a shared preponderance for metastasis to a specific organ - for example, liver metastasis in both melanoma and colorectal cancer, suggests that target-organ specific adaptations occur and may be determined by the required metabolic requirements and phenotypic plasticity[35].

Dissecting the molecular underpinnings of LM has been challenging due to limited pre-clinical models that recapitulate the liver-metastatic cascade in the presence of an intact immune system. Recent studies using intra-hepatic or portal/splenic vein injections of cancer cells revealed important but narrow aspects of LM biology and growth[36,37]. Here, we leveraged a syngeneic melanoma model that has the potential to develop LM upon tail vein injection, thus, recapitulates several bottle-necks in the LM cascade. We performed functional screens and find that cancer cell intrinsic loss of *Pip4k2c* promotes melanoma

cell metastasis by co-opting an insulin-rich liver milieu via activation of the PI3K/AKT pathway (Fig. 6), without altering primary tumor growth or their metastatic potential to other organ sites (e.g., lung). Importantly, this mechanism may apply for both routes of dual blood supply to the liver, as we demonstrate increased LM via systemic circulation in our melanoma model and a prostate cancer model, and via portal vein, using a colorectal cancer model implanted into the colonic submucosa.

Recent studies demonstrate that hyperinsulinemia, either in the context of insulin resistance or in response to systemic PI3K inhibition, increases tumor growth of subcutaneously implanted patient-derived xenograft models through inhibition of host PI3K[28,38,39]. Our study extends on this observation and shows that insulin-mediated tumor growth disproportionally occurs in LM over primary tumors or other metastatic sites, in line with higher insulin levels in the liver. These effects could be abrogated by reducing the insulin gradient between the liver and other organs through systemic delivery of insulin. Furthermore, combination of systemic PI3K inhibition with either inhibition of SGLT2 or a ketogenic diet could disrupt the effects of host-mediated increase in insulin levels and reduce LM, while having little or no effect on lung metastasis burden. These findings have potential clinical relevance in specific disease contexts. For example, patients with hormone receptor positive breast cancer, for which PI3K inhibitor alpelisib is FDA-approved and ongoing studies test the benefit of adding SGLT2 inhibition or a ketogenic diet (NCT05090358), may particularly benefit from such strategies, when LM are present. While activating mutations of *PIK3CA* are frequent in breast cancer and serve as the basis for the use of PI3K inhibitors in breast cancer, our study suggests that this oncogenic dependency may not be necessary to select patients toward PI3K inhibitor-based combination treatment strategies, thus, expanding the potential pool of patients who may benefit from such therapies.

Our study has potential limitations: Fist, loss or reduced expression of *Pip4k2c* likely represents one example of resulting hypersensitization to insulin, and may have effects beyond regulation of this pathway that we did not measure[40,41]. Our initial screen only targeted kinases, thus, more extensive unbiased approaches are necessary to characterize the entire landscape of potential drivers of LM development. Second, analysis of human data showed that *PIK3CA* mutations are infrequent in melanoma, but enriched in melanoma LM, thus, suggesting that genomic activation of the pathway may directly drive LM in a portion of patients, independent from regulation by *Pip4k2c* or its isoforms. Importantly, even in the presence of PIK3CA mutations, insulin is still required to activate the pathway. Third, transcriptomics analyses of human data may suffer from contamination by normal hepatocytes in LM, and respective parenchymal and infiltrating cells in other analyzed organ sites. However, it is unlikely that this factor had a major effect, as we observed similar pathway enrichment in mouse metastases profiled by single-cell RNA-sequencing, where analyses were restricted to malignant cells. Lastly, further work is required to determine the role of niche cells and the tumor-microenvironment in liver-metastatic organotropism.

Methods

Ethics statement

The research performed in this study complies with ethical regulations. Human specimen research was approved by the Institutional Review Board at Columbia University Irving Medical Center (#AAAO5706). All mouse experiments were performed under IACUC approved animal protocols at Columbia University (AABE6570) and Harvard Medical School (AABQ9616). The maximum subcutaneous tumor size permitted by both IACUCs is 20mm and was never exceeded. Source data is provided for all in vivo experiments.

Mice

6–8 -week-old C57BL/6J (Charles River: 027), NOD/SCID/IL2gR (NSG) (JAX: 005557) and/or BALB/c (JAX: 000651) female mice were obtained from Charles River and/or Jackson Labs. Mice received a normal chow diet (PicoLab Rodent 20 5053 laboratory Diet St. Louis, MO) or a ketogenic diet (Thermo-Fisher AIN-76A) where indicated, with free access to drinking water. Diet composition is described in the Supplementary Table 7. Mice were housed under pathogen-free conditions. Sex was not considered in the study design.

Cell culture

Mouse melanoma cell line HCmel12 was kindly provided by Prof. Thomas Tüting, Magdeburg, Germany. Melanoma cells were grown in ‘complete’ RPMI-1640 medium (Gibson Bioscience) as described previously[13]. RPMI 1640 supplemented with 10%FBS (Gibco™ 10437028), 10mM non-essential amino acids, 1mM HEPES (all from Life Technologies), 20 μM 2-mercaptoethanol (Sigma). Mouse colorectal carcinoma cell line CT26 was cultured in RPMI 1640 medium supplemented with 10% FBS. A375 and HEK293 cells were purchased from ATCC and grown in DMEM supplemented with 10% FBS. Cell lines were routinely tested for mycoplasma contamination using Lonza MycoAlert Kit (Cat. # LT07–318).

Generation of a Cas9-expressing HCmel12 melanoma cells

Cas9 lentivirus was generated from HEK-293T cells transfected with pLX-311Cas9v.2 plasmids (Addgene #118018) and packaging plasmids pMD2.G (Addgene, #12259) and psPAX2 (Addgene, #12260) using TransIT-LT1 Transfection reagent (Mirus). HCmel12 melanoma cells were transduced with Cas9 lentiviral particles followed by blasticidin selection (1μg/ml) for 48 hours. To assess Cas9 cutting efficiency in HCmel12-Cas9 expressing cells, cells were transduced with pXPR_011 (Addgene #59702; gift from John Doench and David Root). Lentivirus expressing EGFP, puromycin resistance and EGFP-targeting sgRNA. Cas9 activity activity was estimated based on the fraction of EGFP-negative cells 7 days later using FACS Canto flow cytometry (BD Biosciences) and analyzed with FlowJo software (TreeStar, v10 for Mac). The fraction of EGFP-negative was used to estimate Cas9 efficiency.

Propagation of Kinome sgRNA libraries and Lentivirus production

Mouse Kinome CRISPR Knockout Library (Brie) was purchased from Addgene (Addgene, #75316), that includes 2,852 sgRNAs targeting 713 kinase genes and 100 control non-targeting sgRNAs (Supplementary Table 3). For library production, HEK293T cells were seeded in DMEM + 10% FBS in T175 flasks one day prior. At 80% confluency, cells were transfected with the Brie library and the packaging/envelope plasmids pMD2.G (Addgene, #12259) and psPAX2 (Addgene, #12260) using TransIT-LT1 Transfection reagent (Mirus). After 6 hours media was replaced with DMEM + 20% FBS, and virus was collected after 48 hours, filtered, and stored at -80 °C.

In vivo CRISPR-Cas9 screen

HCmel12-Cas9 melanoma cells were transduced at a MOI < 0.1 with Brie lentivirus at ≥1000 cells/construct per infection replicate (~$3x10^7$ pre replicate). Cells were spin-infected at 1000 x g, 37°C for 2 hours and incubated for 16 hours followed by a media change. On day 2 post transduction the cells were put into Blasticidin selection (1 μg/ml) for 7 days and Puromycin (1 μg/ml) for the remainder of the experiment. On day 14, $3x10^6$ of library-transduced HCmel12-Cas9 cells were injected into the right flank or lateral tail vein of the mice. In parallel cells were kept in culture for 21, 28, 35, 42, 49,52 days. Tumor growth and signs of sickness were monitored over time. Mice were euthanized after 4 weeks and tumors and metastases were evaluated for metastasis presence, lesions were dissected for gDNA isolation, sgRNA amplification, and sequencing. Genomic DNA was extracted using Qiagen DNeasy Blood & Tissue Kit (69506, Qiagen). sgRNA amplification and sequencing library construction were performed as described previously[15], and sgRNA library was sequenced on a Illumina HiSeq2500 Instrument. CRISPR–Cas9 screens were analyzed and visualized using software packages MAGeCK and MAGeCKFlute R (v4.0.3)[42].

Generation of KO, knockdown and gene-overexpressing cell lines

Individual tumor cell KOs were generated using Cas9 ribonucleoproteins (RNPs) nucleofection as described previously[43]. Target sequences were designed using CHOP-CHOP tool (https://chopchop.cbu.uib.no) or sequences were derived from the original kinome library (sequence information in Supplementary Table 8). For insulin receptor knockdown experiments doxycycline-inducible shRNA was used as described previously[28] (Sequence information in **Extended Data Table 8**. Briefly, knockdown of insulin receptor was achieved using a doxycycline-inducible shRNA strategy. For generation of miR-E shRNAs, 97-mer oligonucleotides were purchased coding for predicted shRNAs using Splash RNA, http://splashrna.mskcc.org/27. Oligonucleotides were PCR amplified using the primers miRE-Xho-fw (5′-TGAACTCGAGAAGGTATATTGCTGTTGACAGTGAGCG-3′) and miRE-Eco-rev (5′-TGAACTCGAGAAGGTATATTGCTGTTGACAGTGAGCG-3′). To generate full-length and N-terminal mutant *Pipk4k2c* overexpression constructs, open-reading frames were cloned into pLX305 using Gateway cloning (Supplementary Table 8). Human pDONR223-PIP5K2C (Addgene, #23450) and N-terminal mutant human *PIP4K2C*, ORF were cloned into pLX307 using Gateway cloning and Gibson cloning, respectively. All vectors were sequence verified using Sanger sequencing followed by whole plasmid sequencing.

Proliferation assay

1000 cells were seeded in 96-well plates. After 1, 2, or 3 days of proliferation, cells were fixed in 4% PFA and stained with DAPI. Timepoint zero was used as a reference control. Images were acquired on IVOS microscope, and analysis was performed using Cell Profiler software (https://cellprofiler.org).

Transwell migration assay

Migration was assessed using transwell assays. 2×10^4 melanoma cells pre-treated with insulin were placed in the upper compartment of a transwell chamber with 8.0 μm pore size (Corning, 3422) containing 300 μl (top) and 700 μl media in the lower chamber. Cells were led to adhere and transmigrate through the membrane at 37 °C 5% CO2. Wells treated with no insulin served as controls. After 16 hours, transmigrated cells on the lower surface of the membrane were stained with CFSE, fixed with 4% paraformaldehyde and the mean number was counted in 5 high power fields using Inverted Microscope (Olympus).

Immunoblots

Cells were lysed in 1x Laemmli buffer (10,000 cells per μl) followed by 5min incubation at 95°C. Lysates were separated by 10% SDS–gel electrophoresis and transferred to a PVDF membrane (IB24001, Fisher Scientific). Membranes were blocked for 1 h (11921673001, Roche blocking buffer) in Tris-Buffered Saline, pH 7.6 (TBS, S196830–2, Agilent Technologies) and probed with primary antibodies overnight at 4°C followed by 1h incubation in secondary antibodies at RT. Proteins were detected using the Odyssey CLx Imaging system (LI-COR Biosciences). Antibody information is provided in the Reporting Summary of the paper. Membranes were stripped using Stripping Buffer (46430, Thermo Scientific). Full blots corresponding to the immunoblots shown in the main and supplementary figures are provided as **a Source File**.

RNA isolation, RNA sequencing and analysis

$2x10^6$ parental and *Pip4k2c*^{KO} HCmel12 melanoma cells were plated in 6-well plates FBS-free media overnight, with three biological replicates per condition, total 12 samples. The next day cells were treated with insulin (125ng/ml) for four hours (Supplementary Table 4). RNA was extracted using Qiagen kit (74136) and sequenced on a HiSeq2500 (Illumina). Transcripts were quantified with Salmon[44] using the mouse reference genome release GRCm38.97. The tximeta R package (v.4.3)[45] was used to import transcript-level counts and aggregate them by gene. DESeq2 package was applied to generate normalized gene counts. Gene set enrichment analysis (GSEA) for pathway genes was identified using BROAD java GSEA software with normalized gene counts as input (https://www.gsea-msigdb.org/gsea/index.jsp).

In vitro drug treatment

Cells were washed 1x in PBS, placed in FBS-free media overnight, and treated for 1h with PI3K inhibitors (Pictilisib/GDC-0941 (S1065) and Alpelisib (S2814) from Selleck Chemicals) as indicated with insulin for 15 min before collection for immunoblotting. To

induce insulin receptor knockdown cells were treated with 1μg/ml doxycycline (D9891–5G, Sigma) for 48 hours, washed 1x with PBS, and subjected to signaling studies.

Animal metastasis and drug treatment studies *in vivo*

$5x10^5$ HCmel12 mouse melanoma cells, $1x10^5$ A375 human melanoma cells were injected into the lateral tail vein. Mice were monitored over three to four weeks. When mice showed signs of sickness, 20% of weight loss, impaired activity, hunching, and limb paralysis, animals were euthanized, and organs were harvested for evaluation on metastasis presence. For *in vivo* drug treatment studies, Pictilisib (GDC-0941, HY-50094) and Canagliflozin (JNJ 28431754, HY-10451) were purchased from Medchem Express (Monmouth Junction, NJ). The day after tumor cells injection mice were given vehicle control or treated (daily, 5 out of 7 days) with GDC-0941 (100 mg/kg) or SGLT2i (6 mg/kg) prepared in 'CMC' solution, 0.5% carboxy-methyl-cellulose sodium (CMC, C9481–500G, Sigma) in distilled water supplemented with 0.2% Tween-80 (BCBW1801, Sigma) for the duration of the experiment unless otherwise stated. To maintain *Insr* knockdown *in vivo*, mice bearing $Pip4k2c^{KO}$ cells with dox-inducible *Insr* shRNA were administered 3 mg/kg of doxycycline (Sigma, D3072) intraperitoneally daily, for three to four weeks. Ketogenic diet was started 10 days prior to tumor cell injection where indicated. In experiments combining GDC-0941 and SGLT2 inhibitor (Canagliflozin), the latter was administered 60 min prior to GDC-0941[28] administration. $2x10^5$ tumor cells were injected subcutaneously and tumor growth was monitored over time. When tumors were palpable mice were treated with GDC-0941 (100mg/kg) alone or in combination with SGLT2i (6mg/kg), 3 times a week until the end of the experiment. Mice were euthanized and tumor growth was evaluated.

Endoscopy-guided orthotopic tumor transplantation and injections

Orthotopic injections of CT26 cells was performed as described previously[46]. Briefly, cell lines were split 2 days prior. On the day of injection, cells at 80–90% confluency were harvested by TrypLE Express enzyme (Gibco, 12604013). Tumor cells were resuspended in PBS + 10% Matrigel at $2x10^6$/ml. 100μl was injected into the colon sub-mucosa of each BALB/c recipient mouse by optical colonoscopy using a Hamilton syringe (7656–1) and a custom 33G needle (Hamilton, custom made similar to 7803–05, 16", Pt 4, Deg 12). Successful injections were confirmed by observing large bubbles in the colon mucosa. After 14 days mice were euthanatized and organs evaluated for metastasis presence. Optical colonoscopy was performed two weeks later to assess tumor formation using a Karl Storz Image 1 HD Camera System, Image 1 HUB CCU, 175-Watt Xenon Light Source, and Richard Wolf 1.9mm/9.5 Fr Integrated Telescope (part number 8626.431). One injection was performed per mouse.

Implantation of Insulin Pads in NSG mice

NSG mice were implanted with 2x3 mm slow-release insulin pellets (LinBit - LinShin, Canada) on the dorsum under the skin. Under isoflurane anesthesia, mice were shaved, the surface of the skin treated with a 70% isopropyl alcohol and a lidocaine-based cream (e.g. Emla). The insulin pellet was inserted using 12G trocar and the skin opening is sealed with a drop of Vetbond. After a day, $1x10^5$ tumor cells were injected via lateral tail vein and tumor metastatic burden was evaluated after four weeks.

Blood glucose, C-peptide and tissue insulin measurements

10 μl of blood was taken from the tail of mice before treatment and at indicated time points (15, 30, 60, 90, 120,180, 240 min) and blood glucose was measured using a Prodigy AutoCode Glucometer. At the end point >100 μl of blood was drawn from the mice into heparin coated tubes (07980, Stem Cell Technologies). Blood was centrifuged (10,000g for 10 min at 4 °C), and plasma was stored at −80 °C. Mouse and human C-peptide levels in plasma and mouse insulin levels in liver and lung tissue were measured using commercial ELISA kits (Mouse C-peptide ELISA: 80-CPTMS-E01 (ALPCO); STELLUX Chemiluminescence Human C-peptide ELISA: 80-CPTHU-CH01 (ALPCO); Salem, NH; Insulin: Invitrogen cat. #EMINS).

Tissue collection

Liver and lung tissue were collected immediately after mice were sacrificed, and snap-frozen in liquid nitrogen. For tissue protein isolation, 5mg of powdered liver and lung tissue were homogenized in 300μl Mammalian Protein Extraction Reagent (catalog number: 78501) buffer with proteinase inhibitors (catalog number: 1861281) and incubated at 4 °C for 2 hours with rotating, followed by 20min spin at 20.000g, 4 °C. Supernatant was collected and stored at -80°C.

FDG-PET

C57/BL6 mice were injected with *Pip4k2c*^{KO} melanoma cells. After 3 weeks mice were scanned for liver metastasis presence using PET with [F18] fluorodeoxyglucose (FDG) tracer. At the time of peak blood insulin feedback 60 min post-GDC-0941 injection animals were injected IV with FDG. 60 min later mice were placed into a 4-mouse bed and 30 min static PET images were acquired using a PET scanner (Siemens, Munich, Germany) followed by micro CT (MILabs, Houten, Netherlands) on the same bed for anatomical references. Regions of interests (ROI) were manually drawn over metastases. All PET images were reconstructed using the 3D-OSEM algorithm with 3-iterations in 256 x 256 matrix (Inveon, Siemens, Munich, Germany) and analyzed using VivoQuant ver 4 (Invicro, Boston, MA, USA).

Single cell RNA-sequencing

C57/BL6 mice were injected 5x10^5 HCmel12 melanoma cells via lateral tail vein and euthanized after 21 days with organs harvested and evaluated for metastases presence. (Supplementary Table 4). Around 1x10^4 cells per channel were loaded on a Chromium controller (10x genomics, Pasadena, CA). Sequencing libraries were prepared using standard protocols, and libraries were sequenced on a NovaSeq with S4 flow cell (Illumina, San Diego, CA) and 2x100 bp paired end reads.

Single Cell Computational Analyses

Pre-processing, cell selection and filtering of individual scRNA-seq samples.—CellRanger (v6.0.2) was used to construct a count matrix from raw reads by demultiplexing samples, aligning to refdata-gex-mm10–2020-A, processing barcodes, and collapsing reads with the same unique molecular identifier (UMI), cell barcode and gene

annotation. This matrix was then imported into scanpy[47] (v1.7.2) for sample demultiplexing and analysis. 38 redundant genes were combined by summing the molecule counts. Several filtering steps within each sample were performed to ensure high data quality. Viable cells were determined based on library size (total molecule counts). Specifically, cells were ranked by library size in descending order, the normalized cumulative sum was computed based on the average of a 10-cell rolling window, and the inflection point was identified using the second derivative. All cells with a library size less than 0.9X the inflection point were discarded (Extended Figure 4a). Additionally, cells with > 20% mitochondrial transcripts (Extended Figure 4b), with low coverage defined by

$$\frac{reads}{molecule} < \mu\left(\frac{reads}{molecule}\right) - 2.5 \times std\left(\frac{reads}{molecule}\right)$$

or with low complexity libraries (in which detected molecules align to a small subset of genes determined by at least 0.4X standard deviations from a linear fit) (Extended Figure 4c) were discarded. Scrublet[48] was used to predict cell doublet scores using an expected doublet rate of 0.06. The filtered count matrix was normalized by library size and scaled by a constant of 10,000. The matrix was then log-transformed using: $log_{10}(x; + 0.1) - log_{10}(0.1)$.

Merged sample library generation.—After processing and filtering individual samples, 16 murine tumor samples were mergered, totaling 98,126 cells with a median library size of 2,065 transcripts each. Genes detected in fewer than 5 cells (n = 12,621) were excluded. Using the infection point of the smoothed doublet score distribution as a threshold, 2,520 suspected doublet cells were eliminated (2.6%), resulting in 95,606 high-quality cells expressing 19,624 genes with 3,739 highly variable genes (HVGs). Cell library size and mitochondrial content were consistent across samples (Extended Figure 4d). CellAssign was used to identify tumor cells based on cell type-specific markers, revealing 1,227 tumor cells (n = 1,124 liver and n = 103 lung metastasis cells) (Extended Data Fig. 4e). Tissue-specific cell type-marker genes were assembled using the Mouse Cell Atlas (MCA)[49] and Human Cell Lung Atlas (HCLA)[50] (described and annotated in Supplementary Table 5) and supplemented by canonical markers curated from the literature (e.g. *Ngfr* for basal cells[51], *Scgb1a1* for secretory/club cells[52], and pigmentation-associated genes: *Mitf*, *Mlana*, *Dct*, *Tyr*, and *Tyrp1* to distinguish melanoma cells[8]).

Data Visualization—Tumor cells and marker genes were visualized using UMAP in scanpy[53] after selecting 34 PCs, based on the plateau of the cumulative explained variance, and the default k=15 nearest neighbors (Extended Data Fig. 4e). To compare transcriptional states in the liver and lung metastases, differential gene analysis was performed using Seurat's (4.1.1)[54] Wilcoxon rank-sum test for differential gene expression with Bonferroni correction (Extended Data Fig. 4f). To detect biological processes associated with the tumor cells from each metastatic site, GSEA of MSigDB[55] pathways was performed (Hallmark genes, KEGG, Gene Ontology Biological Process, and Wikipathways) via ClusterProfiler (v3.16.1)[56] for all DEGs ranked by $-log10(pval)*sign(avg\_log2FC)$ (Extended Data Fig. 4e).

Bulk RNA-seq

RNA was extracted from 15 human liver metastasis samples (Supplementary Table 4). Tumor areas were macro-dissected and RNA was extracted using Qiagen kit All Prep DNA/RNA FFPE Kit (Catalog Number 80234), quantified using Qu-bit and stored at -80 °C until use.

Poly-A pull-down was used to enrich mRNAs from total RNA samples, followed by library construction using Illumina TruSeq chemistry. Libraries were then sequenced using an Illumina NovaSeq 6000 at Columbia Genome Center. Samples were multiplexed in each lane, which yielded targeted number of paired-end 100bp reads for each sample. RTA (Illumina) was used for base calling and bcl2fastq2 (v 2.19) for converting BCL to fastq conversion, coupled with adaptor trimming. Pseudoalignment to a kallisto index created from Human transcriptomes GRCh38 was performed using kallisto (0.44.0)[57]. This resulted in 15 liver metastases (LM15) samples. This data was combined with the MET500 effort[30]. The MET500 RNAseq data and sequencing sample metadata were downloaded from https://xenabrowser.net/datapages/?cohort=MET500%20(expression%20centric) on 2022-07-21. The MET500 fragments per kilobase of transcript per million mapped reads values (FPKM) were converted to transcripts per million (TPM) to be consistent with LM15. For main figure analyses Met500 samples were filtered to samples with annotated tumor content greater than 0.5. This filter increased to 0.7 for extended data figure analyses. The 0.5 cutoff led to 237 Met500 samples, including 93 liver, 16 lung, and 159 non-liver metastases, while the 0.7 led to 141 Met500 samples, including 56 liver, 9 lung, and 100 non-liver metastases. (Supplementary Table 5). The MET500 and LM15 TPM matrix were combined, keeping genes that existed within both datasets. The MET500 samples and LM15 samples were integrated using ComBat-seq[58]. This was followed by dimensional reduction using PCA to ensure proper integration. Only genes characterized as ‘protein_coding’ were included, using biomaRt to download Ensembl biotype annotations. Genes that were nonzero in 25% or more of samples were excluded, resulting in 17,281 genes for downstream testing. Differentially expressed genes (DEGs) were found by running a Wilcoxon rank-sum test (wilcox.test() function in R) on the expression between comparison groups. GSEA was performed using fgsea[59] on the on the list of DEGs ranked by -log10(fdr) * sign(log2_fold_change). Gene sets of interest included Cancer Hallmarks gene sets from MSigDB and the Kyoto Encyclopedia of Genes and genomes, along with select pathways from WikiPathways and Gene Ontology Biological Process[60,61,55].

Arriaga dataset analysis.—For validation of these results in a separate NPK^{EYFP} mouse model, bulk RNA-seq data from Arriaga cohort[29] was used. All available data from liver (n=7), lung (n=14) and bone metastases (n=15), and primary tumors (prostate, n=22) were analyzed. For differential expression analysis, raw count data was input in DESeq2. GSEA was performed using the same methods and gene sets as previously described.

Exome/RNA-seq and analysis through Caris Life Sciences

Next-generation sequencing (NGS) was performed on genomic DNA isolated from micro dissected FFPE tumor samples using the NextSeq or NovaSeq 6000 platforms (Illumina, Inc., San Diego, CA). For NextSeq sequenced tumors, a custom-designed SureSelect XT

assay enriched 592 whole-gene targets (Agilent Technologies, Santa Clara, CA). NovaSeq whole exome sequenced tumors utilized a hybrid pull-down panel of baits targeting over 700 clinically relevant genes at high coverage, along with another panel enriching for additional >20,000 genes at a lower depth. A 500Mb SNP backbone panel (Agilent Technologies) aided gene amplification/deletion measurements. All variants were detected with > 99% confidence, an average sequencing depth of coverage of > 500 and an analytic sensitivity of 5%. This test has a sensitivity to detect as low as approximately 10% population of cells containing a mutation in all exons from the high read-depth clinical genes and 99% of all exons in the 20K whole exome regions. Genetic variants identified were interpreted by board-certified molecular geneticists and categorized as 'pathogenic,' 'likely pathogenic,' 'variant of unknown significance,' 'likely benign,' or 'benign,' according to the American College of Medical Genetics and Genomics (ACMG) standards. When assessing mutation frequencies of individual genes, 'pathogenic,' and 'likely pathogenic' were counted as mutations while 'benign', 'likely benign' variants, and 'variants of unknown significance' were excluded. Variants detected were mapped to reference genome (hg19), and bioinformatics tools (BWA, SamTools, GATK, and snpFF) were used for variant calling; germline variants were filtered using databases such as 1,000 genome and dbSNP.

Tumor-specific RNA was extracted from microdissected FFPE specimens with at least 10% tumor content using a Qiagen RNeasy FFPE Kit. RNA quality and quantity were determined using the Agilent TapeStation. Biotinylated RNA baits were hybridized to the synthesized and purified cDNA targets, and the bait-target complexes were amplified in a post-capture PCR reaction. Whole transcriptome sequencing (WTS) on Illumina Novaseq 6500 generated an average of 60M reads. Raw data was demultiplexed by Illumina Dragen BioIT accelerator, trimmed, counted, PCR-duplicates removed, and aligned to human reference genome hg19 by STAR aligner (v.2.7.8a). TPMs were calculated with Salmon expression pipeline. DEGs were determined by calculating log2 fold-change between defined groups, and genes were considered significantly different when adjusted $p < 0.05$. Significantly enriched pathways across disease sites were determined using GSEA to calculate normalized enrichment score and significance level adjusted for multiple hypothesis testing[61].

Tissue metabolomics

6–8-week-old NSG mice were injected via tail vein with 1 x 10^5 A375 human melanoma cells (n=5 mouse per group). Mice were monitored over 3–4 weeks. When mice showed signs of sickness, animals were euthanized, and organs harvested for evaluation of metastases presence. Liver and lung metastases were snap frozen and subjected to downstream analysis.

Extraction: Metabolites were extracted from 50 mg of frozen tissue using a two-step liquid method similar to Sellik et al[62]. Internal standards ($^{13}C_6$-L-Arginine, $^{13}C_5$ L Valine, $^{13}C_2$-Citric acid, $^{2}H_4$-Succinic acid and $^{13}C_6$-Fructose-6-phosphate) were added, followed by homogenization, sonication, and centrifugation. Supernatants were collected, dried, and resuspended.

LC-MS Analysis: Chromatographic separation utilized Agilent 1290 Infinity II Bio LC system with an AdvanceBio MS Spent Media (150 x 2.1 mm, 2.7 μm). The elution employed a gradient at a flow rate of 250 μL/min with water (10 mM ammonium acetate pH 9) as solvent A and acetonitrile/water (90/10; v/v; 10 mM ammonium acetate pH 9) as solvent B. The linear gradient was: 0 min, 90% B; 2 min, 90% B; 12 min, 40% B; 13 min, 20% B; 16 min, 20% B; followed by 9 min for re-equilibration. Column temperature was 35 °C, injection volume was 5 μL. The column temperature was maintained at 35 °C, and sample injection volume was 5 μL.

Mass spectrometric detection was facilitated by coupling the LC system with a Thermo Orbitrap Q Exactive. Ionization in positive and negative modes utilized the HESI II ion source. MS parameters were optimized, with scan ranges of 70–1050 m/z and 70,000 resolution in full scan mode and 17,500 resolution for data-dependent MS2 acquisitions.

Data Analysis: LC-MS data were processed with MS-Dial, using accurate mass and MS2 spectra for compound identification. MS-DIAL metabolomics MSP spectral libraries were employed for identification. For non-targeted analysis, compounds underwent statistical analysis using MetaboAnalyst. Pareto scaling, univariate and multivariate statistical methods (PCA and PLS-DA), and data normalization.

Specifically for TCA cycle and glycolysis compounds, suspected target analysis was conducted. LC-MS data were manually integrated using Skyline, identifying peaks based on accurate mass and MS2 spectra. The peak areas were normalized using $^{13}C_2$-Citric acid as an internal standard.

Statistical analysis

Graphs represent mean ± s.e.m. unless otherwise stated. Statistical analyses were carried out using GraphPad Prism 9 Software (GraphPad Software, San Diego, CA, USA). Results were considered statistically significant when $p < 0.05$ and precise significance levels are indicated for respective comparisons. The figure legends specify the statistical tests used for each data along with the corresponding sample size (n). In the graphs, individual data points are depicted as dots. To account for multiple comparisons, appropriate adjustments were applied as detailed in the figure legends. No statistical methods were used to predetermine the sample size. Sample sizes were instead determined based on historical sample sizes capable of detecting biologically significant differences for certain assays. If no historical data were available, pilot experiments were performed to determine the relative variability of the assay. Data were assumed to be normal, but this was not always formally tested. No data were excluded from analysis. No randomization was performed in the conducted experiments. No sex or gender analysis was carried out. Data collection and analysis was not performed blind to the conditions of the experiments and outcome assessment.

Extended Data

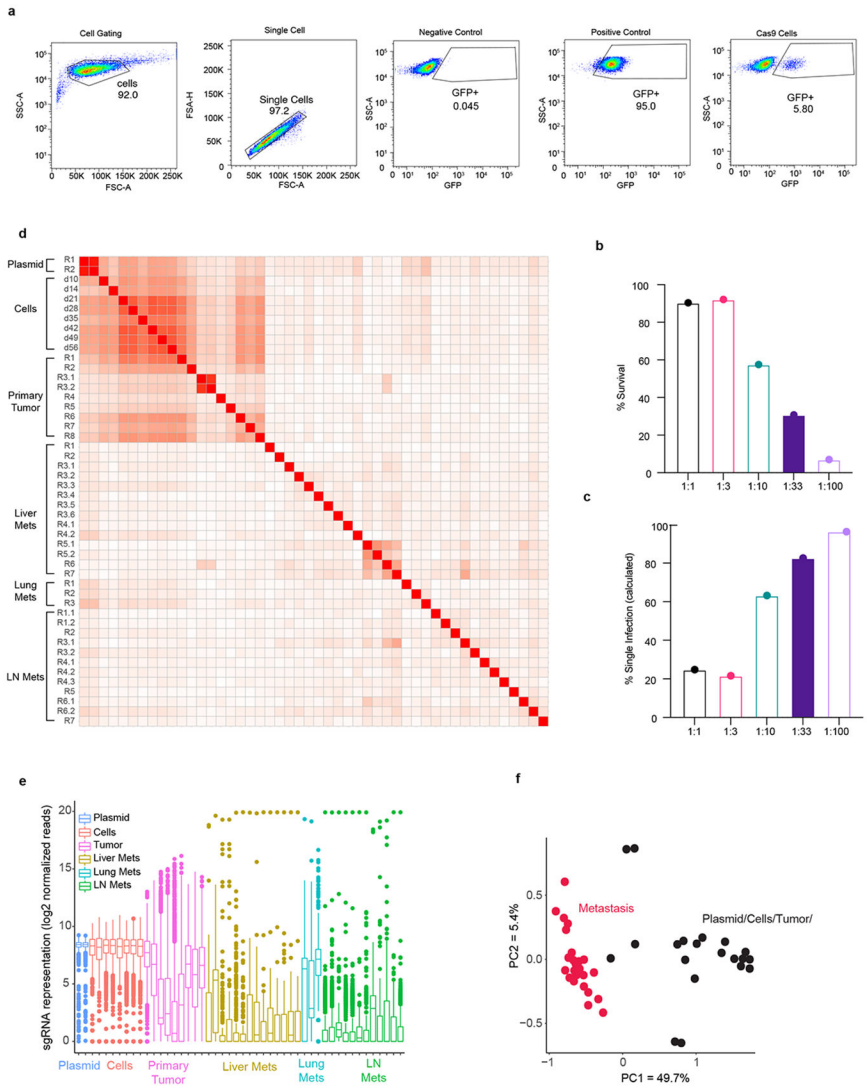

Extended Data Fig. 1. Cas9 expressing HCmel12 melanoma cell line generation, mouse kinome (Brie) library titration and kinome (Brie) sgRNA representation at different steps of tumor cell editing, primary tumor growth, and metastasis.

a, Assessment of Cas9-activity using an EGFP/EGFP-sgRNA-reporter using flow-cytometry in HCmel12 melanoma with Cas9-expression, alongside HCmel12 melanoma cells expressing Cas9 without reporter (negative control), and parental HCmel12 cells without Cas9 but with reporter (positive control). EGFP negative cells (rightmost plot) indicated activity of ~94%. **b,** Transduction of lentiviral library in Cas9-expressing HCmel12 melanoma cells. Percentage of tumor cells (y axis) transduced with the Brie library at virus dilutions (x axis). **c,** Proportion of cells calculated to be infected by one sgRNA-containing viral particle (y axis) at different dilutions of the Brie library (x axis). Filled graphs in **(b,c)** indicate viral concentration/dilution used for the large-scale CRISPR screen. **d,** Pearson correlation coefficient of the normalized sgRNA read counts from Brie plasmid pool, transduced cells in vitro edited over time (10, 14, 21, 28, 35, 42, 49, 56 days after spin

infection), from primary tumors (n=8), from liver (n=14), lung (n=3), and lymph node (n=8) metastases. For each biological sample type, biological replicates (R1, R2, R3… R8), for technical replicates (R3.1, R3.2) are shown. n=8 mice for primary tumors, n=7 mice with Liver mets, n=3 mice with lung mets, n=7 mice with LN mets. **e,** Boxplot of the normalized sgRNA read counts as in (d). Outliers are shown as colored dots for each respective sample. **f,** Principal component analysis (PCA) of normalized sgRNA read counts. X- and y-axis with indicated explained variance of 49.7% and 5.4%, respectively. Samples from Brie plasmid, cells and primary tumors are shown in black while metastases are shown in red. Data is representative of two independent experiments.

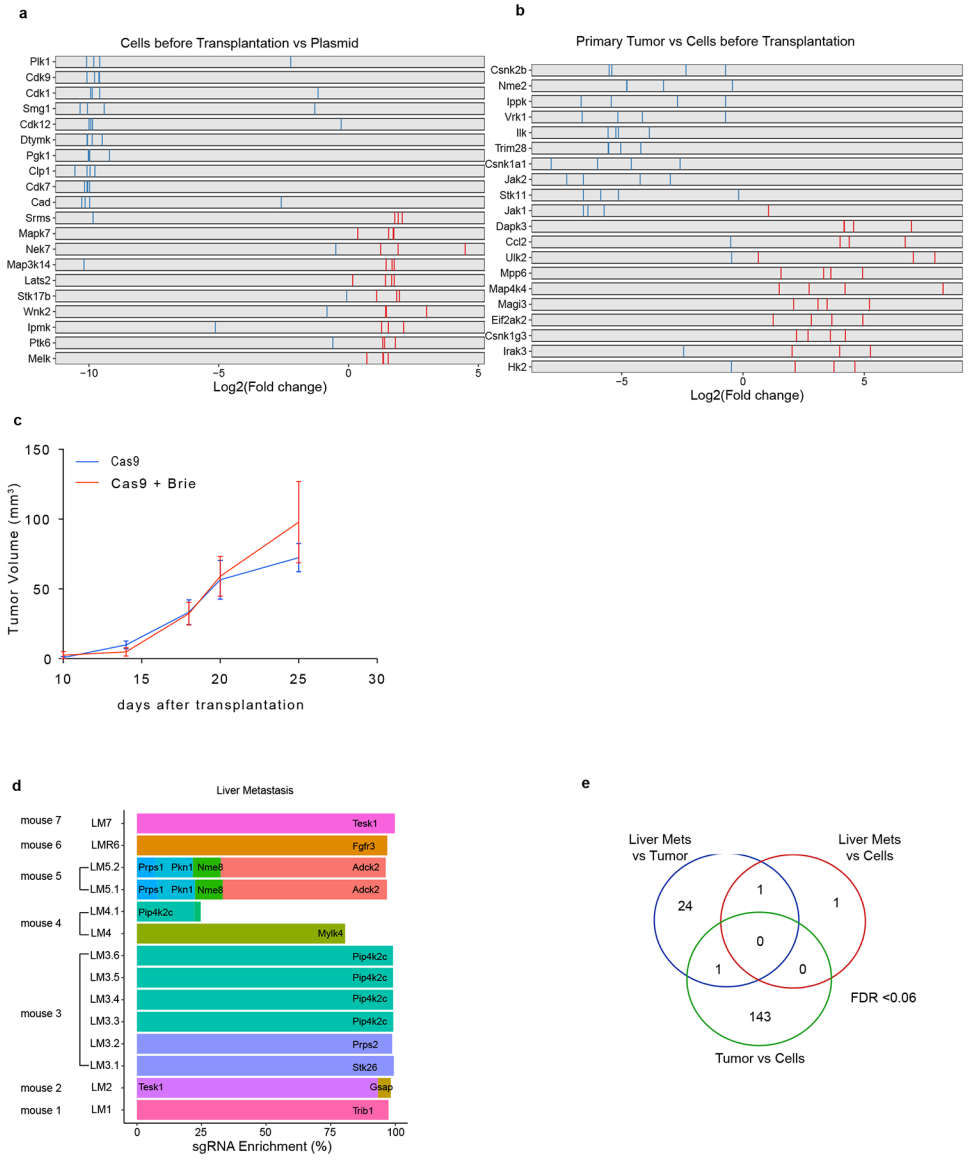

Extended Data Fig. 2. CRIPSR/Cas9 viability screen in HCmel12 melanoma cells in vitro, Identification of essential genes and genes affecting engraftment of tumor cells in vivo followed by Identification of genes affecting liver tropism.

a, b, LFC for all four individual sgRNAs targeting genes enriched (red lines) or depleted (blue lines) in cells vs plasmid **(a)**, and primary tumor vs cells before transplantation **(b)**, are depicted. The top and bottom 10 enriched or depleted genes are labelled with gene symbols. **c,** Tumor growth curves in mice transplanted with Cas9 (n = 5 mice) or Brie-transduced (Cas9 + Brie) HCmel12 melanomas (n = 10 mice) are shown; mean± s.e.m. **d,** Bar graphs showing enrichment of sgRNAs targeted genes in among sgRNAs in liver metastasis. For each of the 14 individual liver metastasis samples (rows) harvested from 7 individual mice, the abundances of sgRNAs reads as a proportion of all reads are shown. Only target genes with at least 2% of the total reads in a sample are shown. e, Venn diagram showing the overlap of enriched sgRNAs in indicated comparisons with FDR < 0.06. Data is representative of two independent experiments.

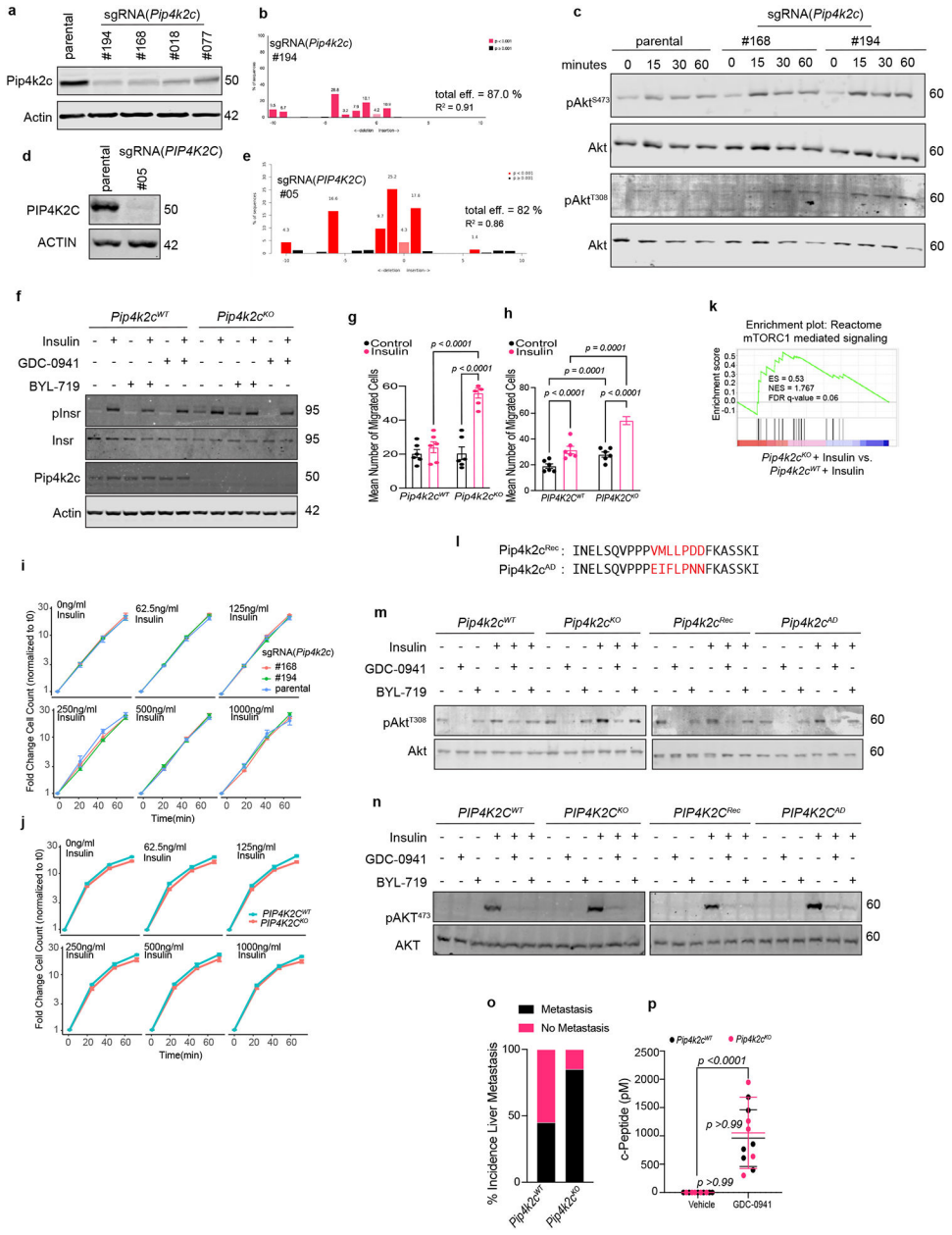

Extended Data Fig. 3. Generation and validation of CRISPR knockout cells *in vitro*.

a, Immunoblot showing efficacy of CRISPR Cas9-mediated knockout of *Pip4k2c* using four sgRNAs. **b,** Resulting insertions/deletions for *Pip4k2c* sgRNA #194 analyzed by Sanger sequencing with Tracking of Indels by Decomposition (TIDE https://tide.nki.nl) and estimated efficiency of Cas9-mediated cuts. **c,** Immunoblots of phosphorylated and total AKT at two phosphorylation sites pAktS473 and pAktT308 in parental and two of *Pip4k2c* KO clones over time. **d,e,** Immunoblot showing efficacy of CRISPR Cas9-mediated knockout of *PIP4K2C* using guide #5 in human A375 melanoma cell lines **(d)** and resulting indels **(e)** as in **(b)**. **f,** Immunoblot of HCmel12 parental or *Pip4k2c* KO cells treated with insulin, and/or GDC-0941 (0.1μM) or BYL-719 (1μM). Blotted is the total abundance of insulin receptor (Insr) and phosrpho-Insr. **g,** Effect of insulin treatment on migration

potential measured by transwell assay. Shown is the mean number of migrated parental and *Pip4k2c* KO cells with and without insulin treatment. n=3 replicates per condition; mean ± s.e.m. **h,** Same as in **(g)** for A375 melanoma cell lines. **i,j,** Proliferation assay of HCmel12 (i) or A375 (j) *Pip4k2c* WT and *Pip4k2c* KO melanoma cells at different insulin concentrations over time. Cell counts were normalized to t0 proliferation is shown as fold change. n=3 replicates per condition; mean± s.e.m. **k,** Gene set enrichment analysis of RNA-seq data comparing *Pip4k2c* KO with parental cells stimulated with insulin. Exemplary pathway enrichment for mTORC1 is shown. **l,** Amino acid sequence of wild-type ORF (top) and allosteric domain deficient (AD) Pip4k2c. **m,n,** Immunoblots showing phosphor-AKT in parental, *Pip4k2c* KO, and *Pip4k2c* KO rescued with either wild-type *Pip4k2c* allele (*Pip4k2c* Rec) or allosteric domain-deficient (*Pip4k2c* AD) and combinatorial exposure to insulin (250ng/ml, first row) and PI3K inhibitor GDC-0941 (0.1μM, second row) or BYL-719 (1μM, third row) in murine HCmel12 **(m)** or human A375 **(n)** melanoma models. Samples are derived from the same experiment and gels/blots were processed in parallel. **o,** Incidence of liver metastasis in mice bearing A375 *PIP4K2C* WT and *PIP4K2C* KO melanoma cells, n=10 mice per group; **p,** C-peptide levels (in pM) for *Pip4k2c* WT and *Pip4k2c* KO HCmel12 tumor-bearing animals with and without GDC-0941 treatment. Plasma was collected after 2 hours of treatment with GDC-0941 and vehicle treatment was used as control, n=5 mice per group. Statistical significance was determined using 2-way ANOVA Tukey's multiple comparisons test for (**g,h,p**). Data is representative of two independent experiments (**g,h,i,j,o,p**). Significance levels as indicated.

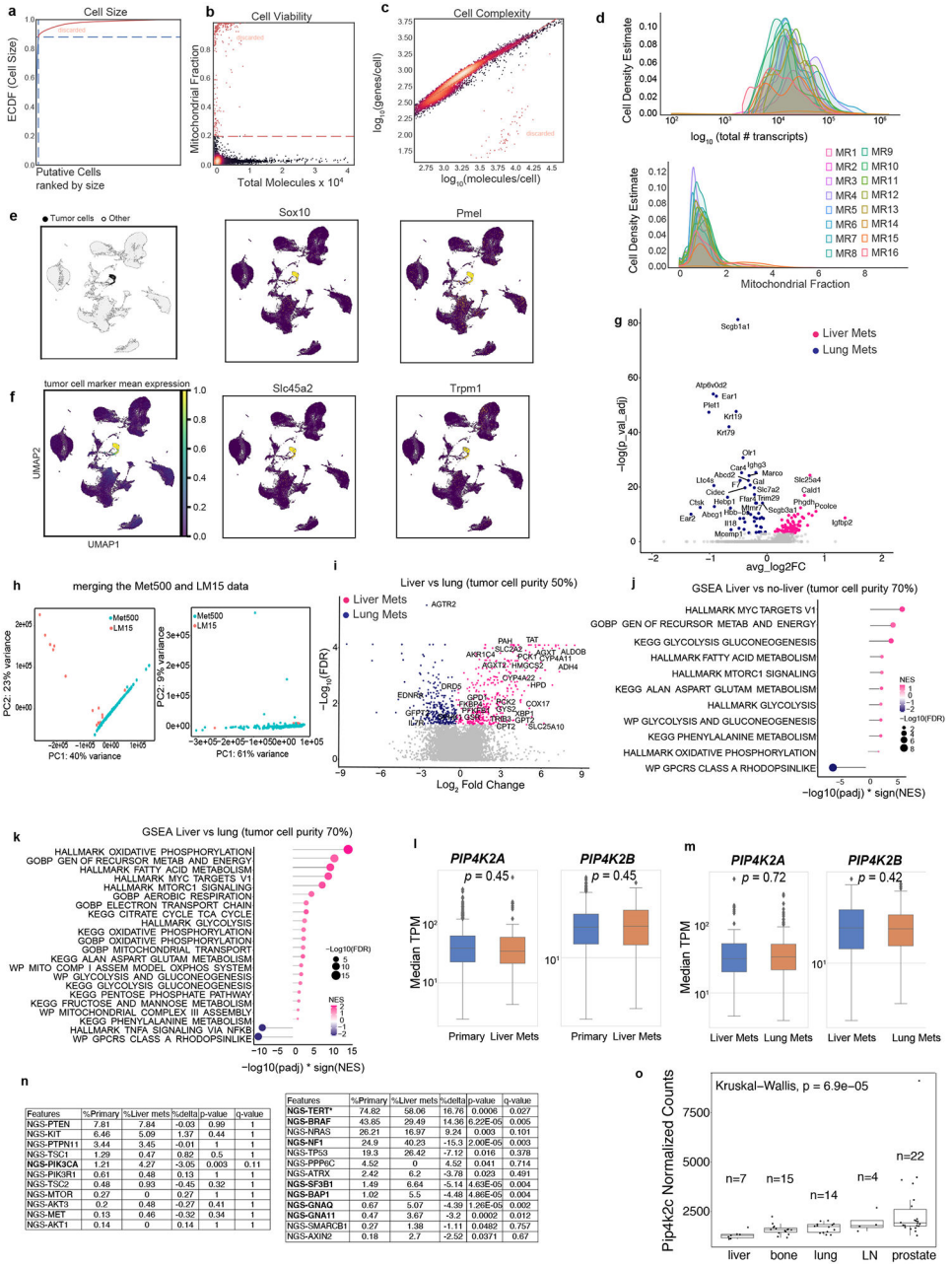

n

Features	%Primary	%Liver mets	%delta	p-value	q-value
NGS-PTEN	7.81	7.84	-0.03	0.99	1
NGS-KIT	6.46	5.09	1.37	0.44	1
NGS-PTPN11	3.44	3.45	-0.01	1	1
NGS-TSC1	1.29	0.47	0.82	0.5	1
NGS-PIK3CA	1.21	4.27	-3.05	0.003	0.11
NGS-PIK3R1	0.61	0.48	0.13	1	1
NGS-TSC2	0.48	0.93	-0.45	0.32	1
NGS-MTOR	0.27	0	0.27	1	1
NGS-AKT3	0.2	0.48	-0.27	0.41	1
NGS-MET	0.13	0.46	-0.32	0.34	1
NGS-AKT1	0.14	0	0.14	1	1

Features	%Primary	%Liver mets	%delta	p-value	q-value
NGS-TERT*	74.82	58.06	16.76	0.0006	0.027
NGS-BRAF	43.85	29.49	14.36	6.22E-05	0.005
NGS-NRAS	26.21	16.97	9.24	0.003	0.101
NGS-NF1	24.9	40.23	-15.3	2.00E-05	0.003
NGS-TP53	19.3	26.42	-7.12	0.016	0.378
NGS-PPP6C	4.52	0	4.52	0.041	0.714
NGS-ATRX	2.42	6.2	-3.78	0.023	0.491
NGS-SF3B1	1.49	6.64	-5.14	4.63E-05	0.004
NGS-BAP1	1.02	5.5	-4.48	4.86E-05	0.004
NGS-GNAQ	0.67	5.07	-4.39	1.26E-05	0.002
NGS-GNA11	0.47	3.67	-3.2	0.0002	0.012
NGS-SMARCB1	0.27	1.38	-1.11	0.0482	0.757
NGS-AXIN2	0.18	2.7	-2.52	0.0371	0.67

Extended Data Fig. 4. Validation of findings in mouse and human metastatic samples using scRNA-seq and Bulk RNA-seq.

a-c, Quality control plots for single cell RNA sequence data. Cells were filtered based on **(a)** cumulative number of transcript counts, **(b)** fraction of mitochondrial mRNA detected per cell and **(c)** cell complexity as described in the methods; shown here for one representative library. **d,** Kernel Density Estimate (KDE) plots showing distribution across cells of total number of transcripts (top) and mitochondrial fraction (bottom) for each sample. **e,f,** UMAP projections showing the tumor cell population, mean log-transformed gene expression of tumor cell marker gene signature, and log-transformed expression of select individual tumor cell marker genes. **g,** Top differentially expressed genes in liver metastasis (pink)

vs lung metastasis (purple) tumor cells. Genes are projected by the $-log10(p\_adj)$ by the $averagelog2(FC)$ and the most significant DEGs are labelled (padj < 0.05, Wilcoxon test). **h,** PCA of LM biopsy data across cancer types from Met500 and additional LM from melanoma patient biopsies (LM15) generated in this study pre- or post-batch correction with ComBat_seq (Methods). **i,** Differentially expressed genes in liver (n=78, Met500; n=15, LM15, pink) vs lung (n=16, Met500, purple) metastases from patients across cancer types. Genes are projected by average log2 Fold Change by the -log10(FDR) with genes significantly enriched (FDR q-value <0.05, Mann-Whitney test) in liver (pink) and in lung (purple) metastasis tumor samples, with specific genes of interest labelled. **j,** Pathway enrichment analysis (FDR q-value < 0.05, GSEA) in liver (n=41, Met500; n=15, LM15, pink) vs non-liver (n=100, Met500, purple) metastases including only with 70% tumor cell purity. **k,** Pathway enrichment analysis (FDR q-value < 0.05, GSEA) in liver (n=41, Met500; n=15, LM15, pink) vs lung (n=9, Met500, purple) metastases including only with 70% tumor cell purity. **l,m,** Expression levels of *PIP4K2A/B* in primary tumors vs. liver metastases **(l)** and liver vs. lung metastases **(m)**. **n,** Frequency of genomic alterations across primary cutaneous melanomas and liver metastases from Caris melanoma patient cohort. The left table summarizes the frequencies between primary tumors and liver metastases for selected genes in the PI3K/AKT pathway, along with adjusted p and q values (methods), and the right table indicates unbiased analyses across all interrogated gene mutations among the same sites. **o,** Expression of *Pip4k2c* in primary prostate cancers, lymph node, lung, bone and liver metastases from the Arriaga et al. cohort; for all boxplots, n refers to the number of samples, and p refers to the p-value. The center line indicates the median, the box limits denote the first and third quartiles, and the whiskers indicate the lowest or highest data points at the first quartile minus or plus 1.5 times the interquartile range. Statistical significance was determined using Frequency of genomic alterations: Mann-Whitney U Two-tailed test for **(l, m)** and chi-square or Fisher's Exact for **(n)**. Significance as indicated.

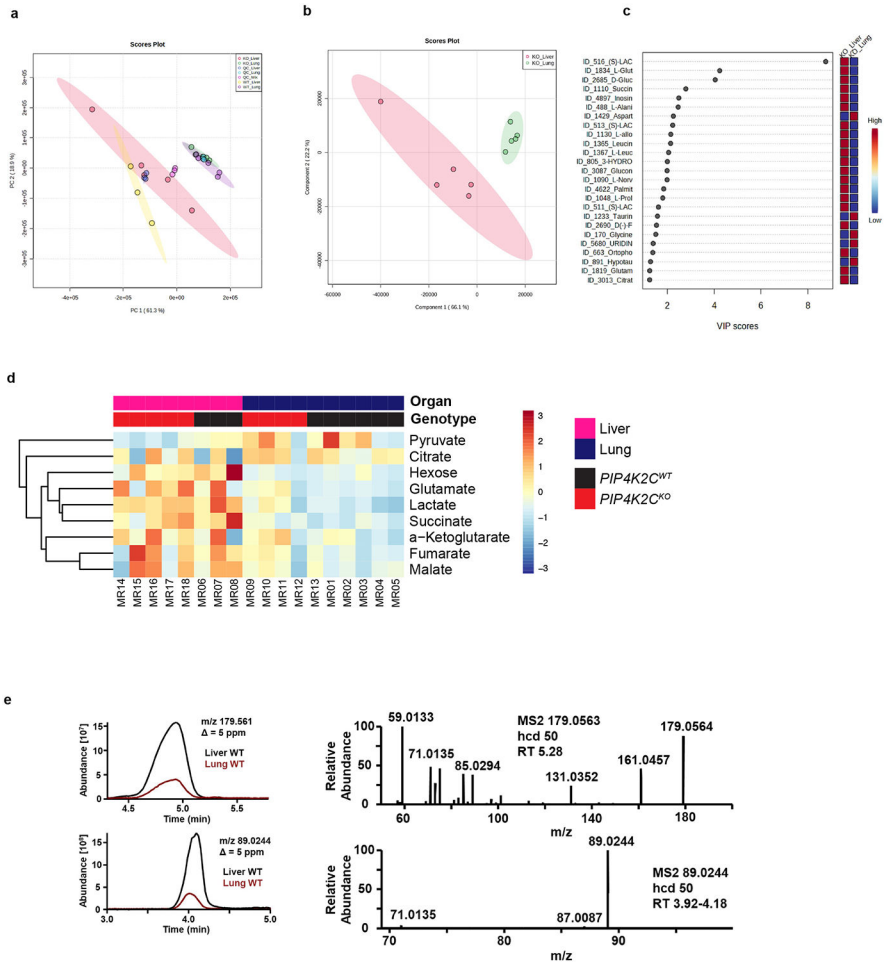

Extended Data Fig. 5. Metastatic site influences tumor cell metabolic state.

a, Score plot of a PCA analysis of all putatively identified metabolites by LC-MS in positive ionization mode. **b,** Score plot of a PLS-DA analysis of putatively identified metabolites by LC-MS in negative ionization mode comparing liver and lung metastatic samples from animals with A375 human melanomas with indicated genotypes (Methods). **c,** VIP score plot generated based on a PLS-DA of putatively identified metabolites by LC-MS in negative ionization mode comparing liver and lung metastatic samples from animals with A375 human melanomas with indicated genotypes, showing a strong change in lactic acid, glutamic acid and a hexose (e.g. glucose) that is causing the separation of the groups in **(b)**. **d,** Heat map of results from a suspected targeted analysis. Compounds were manually identified in the LC-MS data based on MS1 accurate mass and MS2-spectrum. The corresponding peaks were integrated, and the results normalized by 13 C2-Citric acid that was spiked to the sample as an internal standard. The compounds were selected based on the multivariate data analysis indicating a change in the glycolysis and/or TCA cycle. disease site, liver (n=8 specimens) vs. lung (n=10 specimens); and genotype, parental [*PIP4K2C* WT] and *PIP4K2C* KO. Statistical significance was determined using Two-tailed t-test for (d), Lactate (p=2.36727E-05), Pyruvate (p=0.03), Citrate (p=0.25), a-Ketoglutarate (p=0.18), Succinate (p=0.004), Fumarate (p=0.04), Malate (p=0.04), Hexose

(p= 6.72275E-06). **e,** Extracted ion chromatograms (left) and corresponding MS2 spectra of the putatively identified hexose (e.g. glucose) with an accurate mass for the [M-H]- ion of 179.5610 (top) and of lactic acid with an accurate mass for the [M-H]- ion of 89.0244 (bottom). Much lower intensities were detected in the lung samples compared to the liver samples (Right).

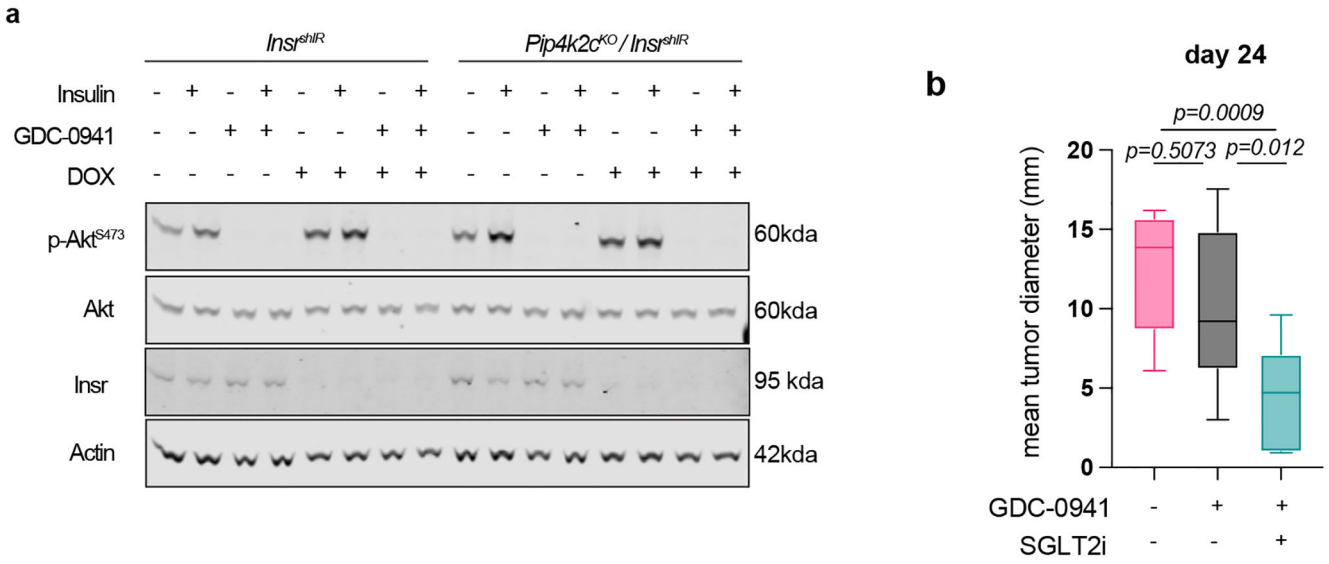

Extended Data Fig. 6. Role of *Pip4k2c* loss in primary tumor growth and response to systemic therapies.

a, Immunoblots in matched cell lines with indicated genotypes (top) and combinatorial exposure to insulin (250ng/ml, first row), PI3K inhibitors GDC-0941 (0.1μM, second row), and Doxycycline (1μg/ml, third row). **b,** Combined tumor diameter at day 24 in treatment groups across genotypes; n=10 mice per condition. Box plots denote the minima, maxima and median. Experiment was repeated twice with similar results. Statistical significance was determined using One-way ANOVA Tukey's multiple comparisons test. Data is representative of two independent experiments **(b)**. Significance levels as indicated.

Supplementary Material

Refer to Web version on PubMed Central for supplementary material.

Acknowledgements

We sincerely thank Stephanie H. Davis, who sadly passed away during the completion of this study, for her dedication to excellence in cancer biology research and her passion for conducting humane animal research. We also thank John Doench (Genome perturbation platform at the Broad Institute) for technical guidance on the *in vivo* CRISPR screen, Dr. Audrey V. Parent from UCSF for technical advice, and Drs. Eunhee Choi, Albert Hung, Snoeck-Hans Wilhelm and Liu Hsiauo-Yun from Columbia University for technical advice. B.I. is supported by National Institute of Health grants, R37CA258829, R01CA280414, R01CA266446, U54CA274506, and additional by the Pershing Square Sohn Cancer Research Alliance Award, the Burroughs Wellcome Fund Career Award for Medical Scientists; a Tara Miller Melanoma Research Alliance Young Investigator Award; the Louis V. Gerstner, Jr. Scholars Program; and the V Foundation Scholars Award. B.N. was supported by K00CA234950. Ma.Rö. is supported by Wilhelm-Sander-Stiftung (2020.100.1); DFG RO 764 15/2; Cluster of Excellence iFIT (EXC 2180) "Image-Guided and Functionally Instructed Tumor Therapies", University of Tübingen, Germany, funded by the Deutsche Forschungsgemeinschaft (DFG, German Research Foundation) under Germany's Excellence Strategy EXC 2180-390900677. E.M.E partially supported by NIH T32 (grant no. GM132083). L.C. is supported by

NIH/NCI grant F30CA281104. S.F.B. is supported by Mark Foundation for Cancer Research (20-028-EDV), Oliver S. and Jennie R. Donaldson Charitable Trust, Mathers Foundation, CSHL Cancer Center Shared Resources (Animal and Histology Core Facilities) and acknowledges support by NCI Cancer Center Support grant P30CA045508. L.C.C. is supported by NCI R35 CA197588. This work was supported by NIH/NCI Cancer Center Support Grant P30CA013696 and MSTP training grant T32GM007367 (for MD/PHD Students). Metabolomics Workbench is supported by NIH grant U2C-DK119886 and OT2-OD030544 grants. The following illustrations were prepared using BioRender.com Fig. 1a, h, Fig.3h, and Fig.6a.

Competing Interests Statement

B.I. has received consulting fees/honoraria from Volastra Therapeutics Inc, Merck, AstraZeneca, Eisai and Janssen Pharmaceuticals and has received research funding to Columbia University from Alkermes, Arcus Biosciences, Checkmate Pharmaceuticals, Compugen, Immunocore, and Synthekine. None of these are relevant to the current work. C.G. has received consulting fees from Watershed Informatics. S.F.B. owns equity in, receives compensation from, and serves as a consultant and the Scientific Advisory Board and Board of Directors of Volastra Therapeutics Inc. L.C.C. is a co-founder, member of the SAB, and holds equity in Agios, Petra, Volastra Therapeutics Inc., Faeth, and Larkspur. These companies are developing novel therapies for cancer, though drugs from these companies are not discussed in this manuscript. DS reports grants (to institution) from Amgen, Array/Pfizer, Bristol-Myers Squibb, MSD, Novartis, and Roche; consulting fees/honoraria from 4SC, Amgen, Array Biopharma, AstraZeneca, Bristol-Myers Squibb, Daiichi Sankyo, Haystick, Immunocore, InFlarX, Innocent, LabCorp, Merck Serono, MSD, Nektar, NeraCare, Novartis, OncoSec, Pfizer, Philogen, Pierre Fabre, Replimune, Roche, Sandoz, Sanofi/Regeneron, and Sun Pharma; support for attendings meetings or travel support from Bristol-Myers Squibb, MSD, Merck Serono, Novartis, Pierre Fabre, and Sanofi; participation on drug safety monitoring or advisory boards for 4SC, Amgen, Array Biopharma, AstraZeneca, Bristol-Myers Squibb, Daiichi Sankyo, Immunocore, InFlarX, Merck Serono, MSD, Nektar, NeraCare, Novartis, OncoSec, Pfizer, Philogen, Pierre Fabre, Replimune, Roche, Sandoz, Sanofi/Regeneron, and SunPharma; and leadership roles for DeCOG, German Cancer Society, Hiege-Stiftung, Deutsche Hautkrebsstiftung, Nationale Versorgungskonferenz Hautkrebs (NVKH) and European Melanoma Registry (EuMelaReg). S.K.D., S.W. and G.S. are employees of Caris Life Sciences. The remaining authors declare no competing interests

Data availability

Gene expression data generated in this study have been deposited in the Gene Expression Omnibus (GEO) under accession number GSE188391. Previously published RNA sequencing data - Arriaga cohort is accessible under accession number GSE143812, MET500 data is accessible at: https://xenabrowser.net/datapages/?cohort=MET500%20(expression%20centric).

The deidentified DNA and RNA sequencing data are owned by Caris Life Sciences and cannot be publicly shared due to the data usage agreement signed by Dr. Benjamin Izar at Columbia University Iriving Medical Center, New York, NY. Qualified researchers can apply for access to these data by contacting Joanne Xiu, PhD at jxiu@carisls.com, submitting a brief proposal, and signing a data usage agreement. Metabolomics data have been deposited in the Metabolomics Workbench (the NIH Common Fund's National Metabolomics Data Repository (NMDR) website, https://www.metabolomicsworkbench.org) under Study ID ST002851 and can be accessed directly via its Project DOI: http://dx.doi.org/10.21228/M8043D .

The remaining data is available within the article or as source data.

References

1. Chaffer CL & Weinberg RA A Perspective on Cancer Cell Metastasis. Science 331, 1559–1564 (2011). [PubMed: 21436443]
2. Gao Y et al. Metastasis Organotropism: Redefining the Congenial Soil. Developmental Cell 49, 375–391 (2019). [PubMed: 31063756]

3. Tsilimigras DI et al. Liver metastases. Nat Rev Dis Primers 7, 27 (2021). [PubMed: 33859205]
4. Lee JC et al. Regulatory T cell control of systemic immunity and immunotherapy response in liver metastasis. Sci. Immunol 5, eaba0759 (2020). [PubMed: 33008914]
5. Tumeh PC et al. Liver Metastasis and Treatment Outcome with Anti-PD-1 Monoclonal Antibody in Patients with Melanoma and NSCLC. Cancer Immunol Res 5, 417–424 (2017). [PubMed: 28411193]
6. Bergers G & Fendt S-M The metabolism of cancer cells during metastasis. Nat Rev Cancer 21, 162–180 (2021). [PubMed: 33462499]
7. Priestley P et al. Pan-cancer whole-genome analyses of metastatic solid tumours. Nature 575, 210–216 (2019). [PubMed: 31645765]
8. Biermann J et al. Dissecting the treatment-naive ecosystem of human melanoma brain metastasis. Cell 185, 2591–2608.e30 (2022). [PubMed: 35803246]
9. Broadfield LA et al. Fat Induces Glucose Metabolism in Nontransformed Liver Cells and Promotes Liver Tumorigenesis. Cancer Research 81, 1988–2001 (2021). [PubMed: 33687947]
10. Moris D, Lu L & Qian S Mechanisms of liver-induced tolerance. Current Opinion in Organ Transplantation 22, 71–78 (2017). [PubMed: 27984276]
11. Lee JW et al. Hepatocytes direct the formation of a pro-metastatic niche in the liver. Nature 567, 249–252 (2019). [PubMed: 30842658]
12. Landsberg J et al. Autochthonous primary and metastatic melanomas in Hgf-Cdk4 R24C mice evade T-cell-mediated immune surveillance. Pigment Cell Melanoma Res 23, 649–660 (2010). [PubMed: 20649939]
13. Bald T et al. Ultraviolet-radiation-induced inflammation promotes angiotropism and metastasis in melanoma. Nature 507, 109–113 (2014). [PubMed: 24572365]
14. Rogava M et al. Tumor cell intrinsic Toll-like receptor 4 signaling promotes melanoma progression and metastatic dissemination. Int. J. Cancer ijc.33804 (2021) doi:10.1002/ijc.33804.
15. Doench JG et al. Optimized sgRNA design to maximize activity and minimize off-target effects of CRISPR-Cas9. Nat Biotechnol 34, 184–191 (2016). [PubMed: 26780180]
16. Zaretsky JM et al. Mutations Associated with Acquired Resistance to PD-1 Blockade in Melanoma. N. Engl. J. Med 375, 819–829 (2016). [PubMed: 27433843]
17. Bakhoum SF et al. Chromosomal instability drives metastasis through a cytosolic DNA response. Nature 553, 467–472 (2018). [PubMed: 29342134]
18. Brognard J, Zhang Y-W, Puto LA & Hunter T Cancer-Associated Loss-of-Function Mutations Implicate DAPK3 as a Tumor-Suppressing Kinase. Cancer Res 71, 3152–3161 (2011). [PubMed: 21487036]
19. Chen S et al. Genome-wide CRISPR Screen in a Mouse Model of Tumor Growth and Metastasis. Cell 160, 1246–1260 (2015). [PubMed: 25748654]
20. LaLonde DP, Brown MC, Bouverat BP & Turner CE Actopaxin Interacts with TESK1 to Regulate Cell Spreading on Fibronectin. Journal of Biological Chemistry 280, 21680–21688 (2005). [PubMed: 15817463]
21. Yang C-S et al. The protein kinase C super-family member PKN is regulated by mTOR and influences differentiation during prostate cancer progression. Prostate 77, 1452–1467 (2017). [PubMed: 28875501]
22. Yang M et al. MYLK4 promotes tumor progression through the activation of epidermal growth factor receptor signaling in osteosarcoma. J Exp Clin Cancer Res 40, 166 (2021). [PubMed: 33980265]
23. Cunningham JT, Moreno MV, Lodi A, Ronen SM & Ruggero D Protein and Nucleotide Biosynthesis Are Coupled by a Single Rate-Limiting Enzyme, PRPS2, to Drive Cancer. Cell 157, 1088–1103 (2014). [PubMed: 24855946]
24. Wang DG et al. PIP4Ks Suppress Insulin Signaling through a Catalytic-Independent Mechanism. Cell Reports 27, 1991–2001.e5 (2019). [PubMed: 31091439]
25. Kim T et al. TRIB1 regulates tumour growth via controlling tumour-associated macrophage phenotypes and is associated with breast cancer survival and treatment response. http://biorxiv.org/lookup/doi/10.1101/2021.06.07.446596 (2021) doi:10.1101/2021.06.07.446596.

26. Soubeyrand S, Martinuk A, Lau P & McPherson R TRIB1 Is Regulated Post-Transcriptionally by Proteasomal and Non-Proteasomal Pathways. PLoS ONE 11, e0152346 (2016). [PubMed: 27019349]
27. Lafitte M et al. FGFR3 has tumor suppressor properties in cells with epithelial phenotype. Mol Cancer 12, 83 (2013). [PubMed: 23902722]
28. Hopkins BD et al. Suppression of insulin feedback enhances the efficacy of PI3K inhibitors. Nature 560, 499–503 (2018). [PubMed: 30051890]
29. Arriaga JM et al. A MYC and RAS co-activation signature in localized prostate cancer drives bone metastasis and castration resistance. Nat Cancer 1, 1082–1096 (2020). [PubMed: 34085047]
30. Robinson DR et al. Integrative Clinical Genomics of Metastatic Cancer. Nature 548, 297–303 (2017). [PubMed: 28783718]
31. Sridhar S et al. Prognostic Significance of Liver Metastasis in Durvalumab-Treated Lung Cancer Patients. Clinical Lung Cancer 20, e601–e608 (2019). [PubMed: 31327642]
32. Tumeh PC et al. Liver Metastasis and Treatment Outcome with anti-PD-1 Monoclonal Antibody in Patients with Melanoma and NSCLC. Cancer Immunol Res (2017) doi:10.1158/2326-6066.CIR-16-0325.
33. Birkbak NJ & McGranahan N Cancer Genome Evolutionary Trajectories in Metastasis. Cancer Cell 37, 8–19 (2020). [PubMed: 31935374]
34. El-Kebir M, Satas G & Raphael BJ Inferring parsimonious migration histories for metastatic cancers. Nat Genet 50, 718–726 (2018). [PubMed: 29700472]
35. Sivanand S et al. Cancer tissue of origin constrains the growth and metabolism of metastases. http://biorxiv.org/lookup/doi/10.1101/2022.08.17.504141 (2022) doi:10.1101/2022.08.17.504141.
36. Yu J et al. Liver metastasis restrains immunotherapy efficacy via macrophage-mediated T cell elimination. Nat Med 27, 152–164 (2021). [PubMed: 33398162]
37. Reichert M et al. Regulation of Epithelial Plasticity Determines Metastatic Organotropism in Pancreatic Cancer. Developmental Cell 45, 696–711.e8 (2018). [PubMed: 29920275]
38. Kalaany NY & Sabatini DM Tumours with PI3K activation are resistant to dietary restriction. Nature 458, 725–731 (2009). [PubMed: 19279572]
39. Nencioni A, Caffa I, Cortellino S & Longo VD Fasting and cancer: molecular mechanisms and clinical application. Nat Rev Cancer 18, 707–719 (2018). [PubMed: 30327499]
40. Zhang Y et al. C24-Ceramide Drives Gallbladder Cancer Progression Through Directly Targeting Phosphatidylinositol 5-Phosphate 4-Kinase Type-2 Gamma to Facilitate Mammalian Target of Rapamycin Signaling Activation. Hepatology 73, 692–712 (2021). [PubMed: 32374916]
41. Triscott J et al. PI5P4Kα supports prostate cancer metabolism and exposes a survival vulnerability during androgen receptor inhibition. Sci Adv 9, eade8641 (2023). [PubMed: 36724278]
42. Wang B et al. Integrative analysis of pooled CRISPR genetic screens using MAGeCKFlute. Nat Protoc 14, 756–780 (2019). [PubMed: 30710114]
43. Frangieh CJ et al. Multi-modal pooled Perturb-CITE-Seq screens in patient models define novel mechanisms of cancer immune evasion. http://biorxiv.org/lookup/doi/10.1101/2020.09.01.267211 (2020) doi:10.1101/2020.09.01.267211.
44. Patro R, Duggal G, Love MI, Irizarry RA & Kingsford C Salmon provides fast and bias-aware quantification of transcript expression. Nat Methods 14, 417–419 (2017). [PubMed: 28263959]
45. Love MI et al. Tximeta: Reference sequence checksums for provenance identification in RNA-seq. PLoS Comput Biol 16, e1007664 (2020). [PubMed: 32097405]
46. Beyaz S et al. High-fat diet enhances stemness and tumorigenicity of intestinal progenitors. Nature 531, 53–58 (2016). [PubMed: 26935695]
47. Wolf FA, Angerer P & Theis FJ SCANPY: large-scale single-cell gene expression data analysis. Genome Biol. 19, 15 (2018). [PubMed: 29409532]
48. Wolock SL, Lopez R & Klein AM Scrublet: Computational Identification of Cell Doublets in Single-Cell Transcriptomic Data. Cell Systems 8, 281–291.e9 (2019). [PubMed: 30954476]
49. Han X et al. Mapping the Mouse Cell Atlas by Microwell-Seq. Cell 172, 1091–1107.e17 (2018). [PubMed: 29474909]

50. Sikkema L et al. An integrated cell atlas of the human lung in health and disease. http://biorxiv.org/lookup/doi/10.1101/2022.03.10.483747 (2022) doi:10.1101/2022.03.10.483747.
51. Rock JR et al. Basal cells as stem cells of the mouse trachea and human airway epithelium. Proc. Natl. Acad. Sci. U.S.A 106, 12771–12775 (2009). [PubMed: 19625615]
52. Rawlins EL et al. The Role of Scgb1a1+ Clara Cells in the Long-Term Maintenance and Repair of Lung Airway, but Not Alveolar, Epithelium. Cell Stem Cell 4, 525–534 (2009). [PubMed: 19497281]
53. Wolf FA, Angerer P & Theis FJ SCANPY: large-scale single-cell gene expression data analysis. Genome Biol 19, 15 (2018). [PubMed: 29409532]
54. Stuart T et al. Comprehensive Integration of Single-Cell Data. Cell 177, 1888–1902.e21 (2019). [PubMed: 31178118]
55. Liberzon A et al. The Molecular Signatures Database (MSigDB) hallmark gene set collection. Cell Syst 1, 417–425 (2015). [PubMed: 26771021]
56. Yu G, Wang L-G, Han Y & He Q-Y clusterProfiler: an R Package for Comparing Biological Themes Among Gene Clusters. OMICS: A Journal of Integrative Biology 16, 284–287 (2012). [PubMed: 22455463]
57. Bray NL, Pimentel H, Melsted P & Pachter L Near-optimal probabilistic RNA-seq quantification. Nat Biotechnol 34, 525–527 (2016). [PubMed: 27043002]
58. Zhang Y, Parmigiani G & Johnson WE ComBat-seq: batch effect adjustment for RNA-seq count data. NAR Genomics and Bioinformatics 2, lqaa078 (2020). [PubMed: 33015620]
59. Korotkevich G et al. Fast gene set enrichment analysis. 060012 Preprint at 10.1101/060012 (2021).
60. Kanehisa M & Goto S KEGG: Kyoto Encyclopedia of Genes and Genomes. Nucleic Acids Res 28, 27–30 (2000). [PubMed: 10592173]
61. Subramanian A et al. Gene set enrichment analysis: a knowledge-based approach for interpreting genome-wide expression profiles. Proc. Natl. Acad. Sci. U.S.A 102, 15545–15550 (2005). [PubMed: 16199517]
62. Sellick CA, Hansen R, Stephens GM, Goodacre R & Dickson AJ Metabolite extraction from suspension-cultured mammalian cells for global metabolite profiling. Nat Protoc 6, 1241–1249 (2011). [PubMed: 21799492]

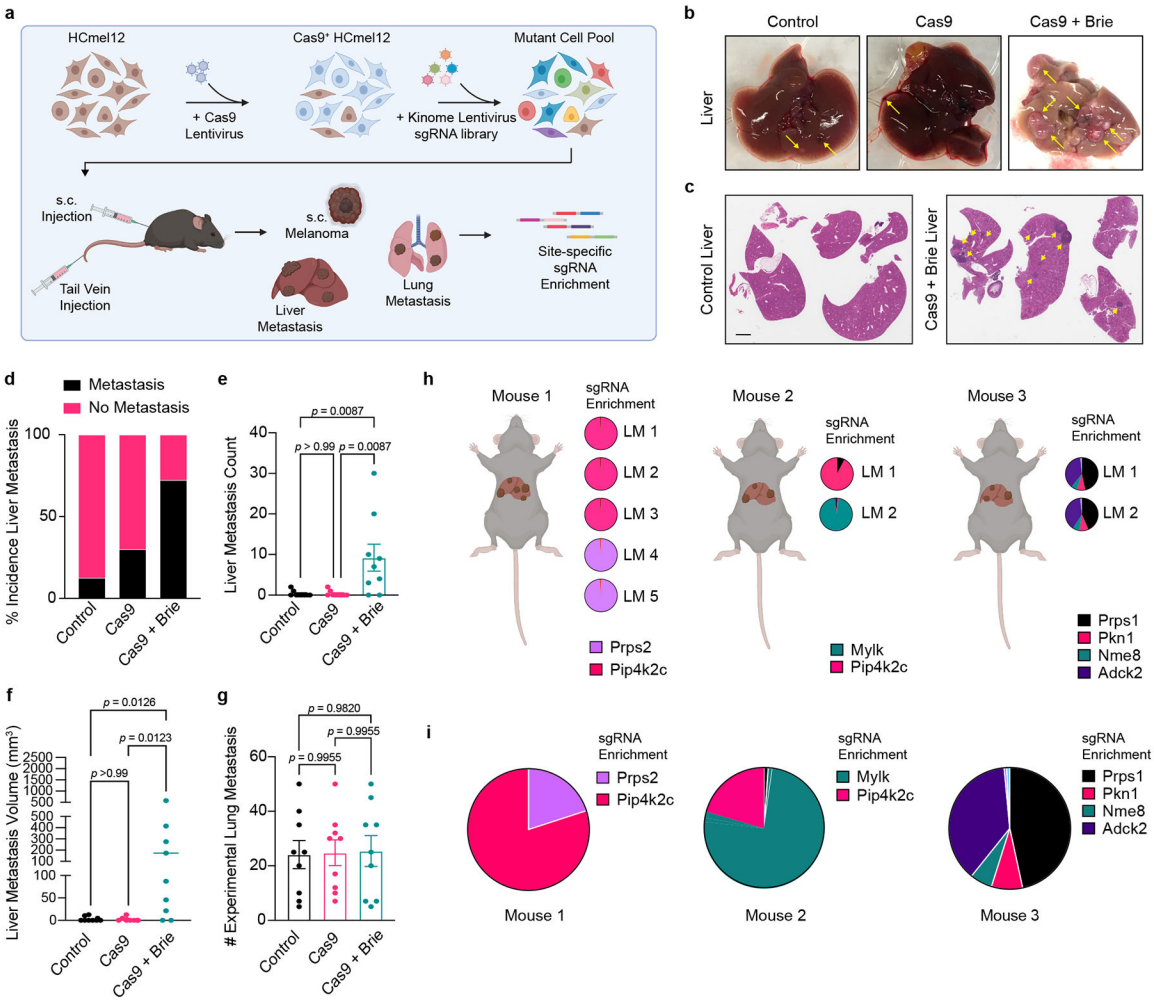

Figure 1. *In vivo* CRISPR-Cas9 screen identifies drivers of liver metastasis.

a, Experimental design of *in vivo* CRISPR-Cas9 screen. **b**, Photographs of representative livers removed from animals in different groups as indicated. Yellow arrowheads indicate pigmented and non-pigmented liver metastases. **c**, Hematoxylin and Eosin staining of representative sections of livers from indicated groups, scale bar 2mm, 40x magnification (n=2 independent experiments). **d**, Stack bar plots indicate fraction of animals bearing liver metastases across different experimental groups. **e,f** Liver metastasis count (e) and calculated liver metastasis disease burden (f) across experimental groups. **g**, Lung metastasis count in corresponding animals from (f); (d-g), n=9 mice per group; bars represent mean ± s.e.m.; One-Way ANOVA Tukey's multiple comparisons test. Data is representative of two independent experiments (d-g). Significance levels as indicated on top of each comparison. **h**, Exemplary distribution of sgRNA read fractions in three animals from the *in vivo* CRISPR-Cas9 metastasis screen. Pie charts show the fraction of the most abundant sgRNAs (sgRNAs with >2% of total reads) in each individual liver metastatic lesion next to each animal. **i**, Summary of fractions of enriched sgRNAs across all lesions from (h) within the individual mouse (larger pie charts below each animal).

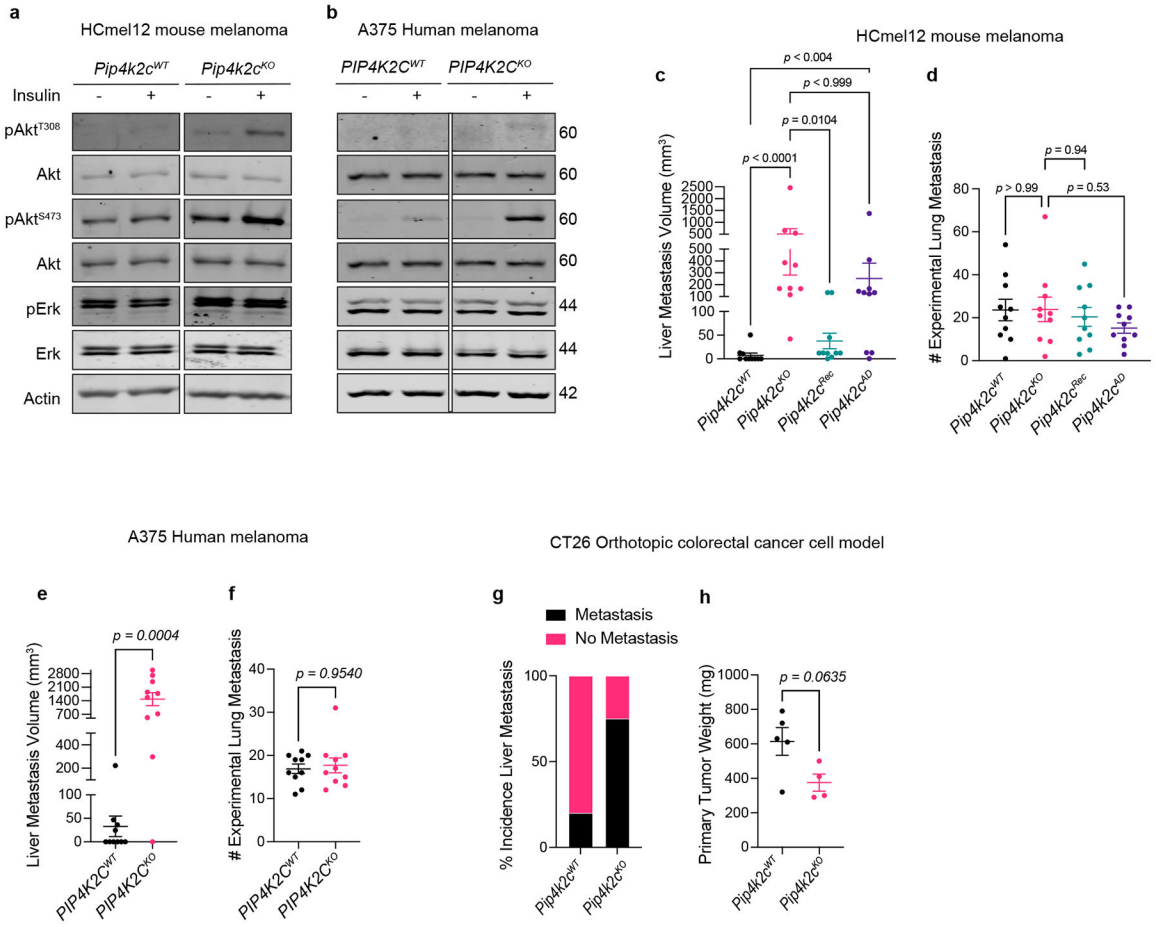

Figure 2. Loss of *Pip4k2c* enhances sensitivity to insulin and promotes liver metastasis, but not lung metastasis.

a,b, Immunoblots showing phosphorylated and total protein of key signaling nodes of pAkt^{S473} and pAkt^{T308} in *WT* or *Pip4k2c*^{KO} cells in (a) HCmel12 and (b) A375 melanoma cell models with (+) or without (-) insulin (250ng/ml) stimulation. **c,d,** Liver metastasis disease burden (in mm^3) and lung metastases count following tail vein injection of parental and *Pip4k2c* KO HCmel12 melanoma in C57BL/6 mice. **e,f,** Liver and lung metastasis burden following tail vein injection of parental and *PIP4K2C* KO A375 melanoma cells in NSG mice. **g**, Incidence of macroscopic liver metastasis in animals following orthotopic injection of parental or *Pip4k2c* KO CT26 colorectal cancer cells in BALB/c mice. **h**, Comparison of tumor weight of primary tumors from experiment shown in (g); (c-f) n=10 mice per group; (g-h) n=4–5 mice per group; mean ±s.e.m. One-Way ANOVA Tukey's multiple comparisons test for (c,d) and Mann-Whitney Two-tailed test for (e-g). Data are representative of three (c,d), two (e,f) or one (h,g) independent experiments. Significance levels as indicated on top of each comparison.

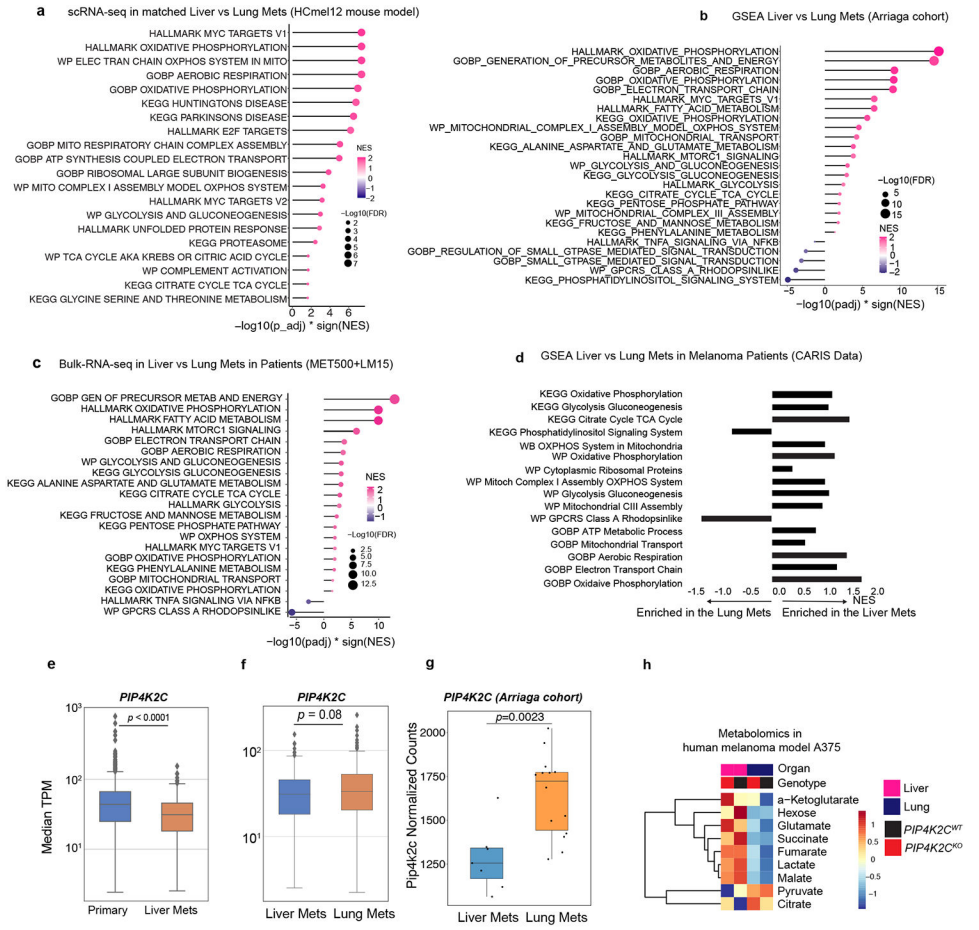

Figure 3. Systemic feedback loop induced by PI3K inhibitor treatment *in vivo* promotes liver organotropism in *Pip4k2c*-deficient tumors in an insulin-dependent manner.

a, Liver metastasis disease burden (in mm^3) upon tail vein injection of parental and *Pip4k2c* KO HCmel12 melanoma cells with and without GDC-0941 treatment (daily, 5 days a week, 100mg/kg). **b**, Lung metastasis burden (metastasis count) in corresponding animals from (a). n = 10 mice per group; mean ±s.e.m; **c**, Blood glucose levels (in mg/dL) in mice following treatment with GDC-0941 or vehicle control over time (minutes). **D**, C-peptide levels (in pM) in corresponding animals from (c); n = 10 mice per group; mean ±s.e.m; 2-way ANOVA Tukey's multiple comparisons test for (a-b) and Mann-Whitney Two-tailed test for (c-d). Significance levels as indicated. **E, f**, Quantification of FDG-μPET (18F-Fluorodeoxyglucose in per cent of injected dose (ID) per gram of (e)) and corresponding liver metastasis uptake (f) 60 min after GDC-0941 administration or vehicle control. Yellow arrows indicate individual liver metastatic lesions. Cardiac FDG-uptake is visualized (asterisk); n=3 mice per group, mean ±s.e.m; unpaired two-sided-t-test (e). **g,** Insulin levels (in pg/ul) in liver and lung tissues from non-tumor bearing mice. n=10 mice per group, mean ±s.e.m; Mann-Whitney Two-tailed test. **h,** Schematic illustrating the insulin pad experiment in mice; **i, j,** Percentage of metastasis surface area in liver (i) and lung (j) of animals implanted with a control pad or insulin pad, and followed by injection of tumor cells via tail vein in NSG mice. **k,** Ratio of lung over liver metastatic burden from experiment in (i,j); n=5 mice per group; mean ± s.e.m; Mann-Whitney Two-tailed test; Data are representative

of three (a-d), two (e-k) independent experiments. Significance levels as indicated on top of each comparison.

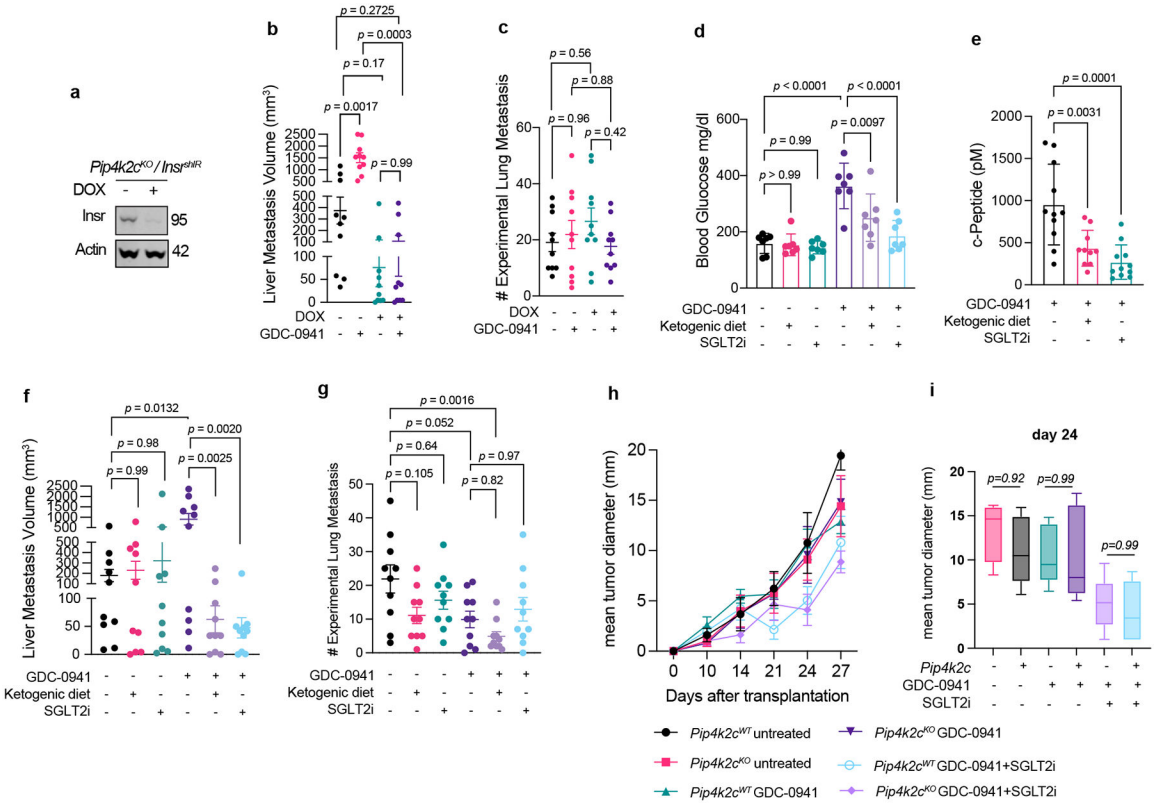

Figure 4. multi-omics analysis of human and mouse liver and lung metastasis.

a, Top enriched pathways (adjusted *p* value < 0.05, top 5 pathways per gene set ranked by NES) of cancer cells isolated from concurrent liver (n=8 specimens, pink) vs lung (n=8 specimens, purple) metastases in mice injected with HCmel12 melanoma cells. **b,** Pathway enrichment (FDR q-value < 0.05) within Arriaga et al., cohort comparing liver (n=7 specimens, pink) vs. lung (n=14 specimens, purple) metastases in a prostate cancer metastasis model. **c**, Enriched pathways (FDR q-value < 0.05) in liver (n=78 patients, Met500; n=15 patients, LM15, pink) vs lung (n=16 patients, Met500, purple) metastases across tumors. **d,** Enriched pathways (adjusted *p* value < 0.05) in liver (n=364) vs lung (n=743) metastases in patients with melanoma tumors; FDR value for GSEA was obtained by Benjamin-Hochberg correction. **e,f,** Expression of *PIP4K2C* in melanoma patient tumors comparing primary cutaneous tumors (n=2,404 patients) vs liver (n=364) (e), and liver (n=364 patients) vs lung (n= 743 patients). Mann-Whitney Two-tailed test. **g**, Expression of *Pip4k2c* from the Arriaga et al., cohort comparing liver (n=7 specimens) vs lung (n=14 specimens), Wilcoxon rank-sum test. For all boxplots, n refers to the number of samples, and p refers to the p-value. The center line indicates the median, the box limits denote the first and third quartiles, and the whiskers indicate the lowest or highest data points at the first quartile minus or plus 1.5 times the interquartile range; Significance levels as indicated. **h,** Cumulative results of selected top differentially abundant metabolites in animals with liver and/or lung metastases following injection with either parental (*PIP4K2C*^{WT}) or *PIP4K2C*^{KO} A375 human melanoma cells; n=5 mice per group; unpaired two-sided-t-test. Lactate (p=2.36727E-05), Pyruvate (p=0.03), Citrate (p=0.25), a-Ketoglutarate (p=0.18), Succinate (p=0.004), Fumarate (p=0.04), Malate (p=0.04), Hexose (p= 6.72275E-06).

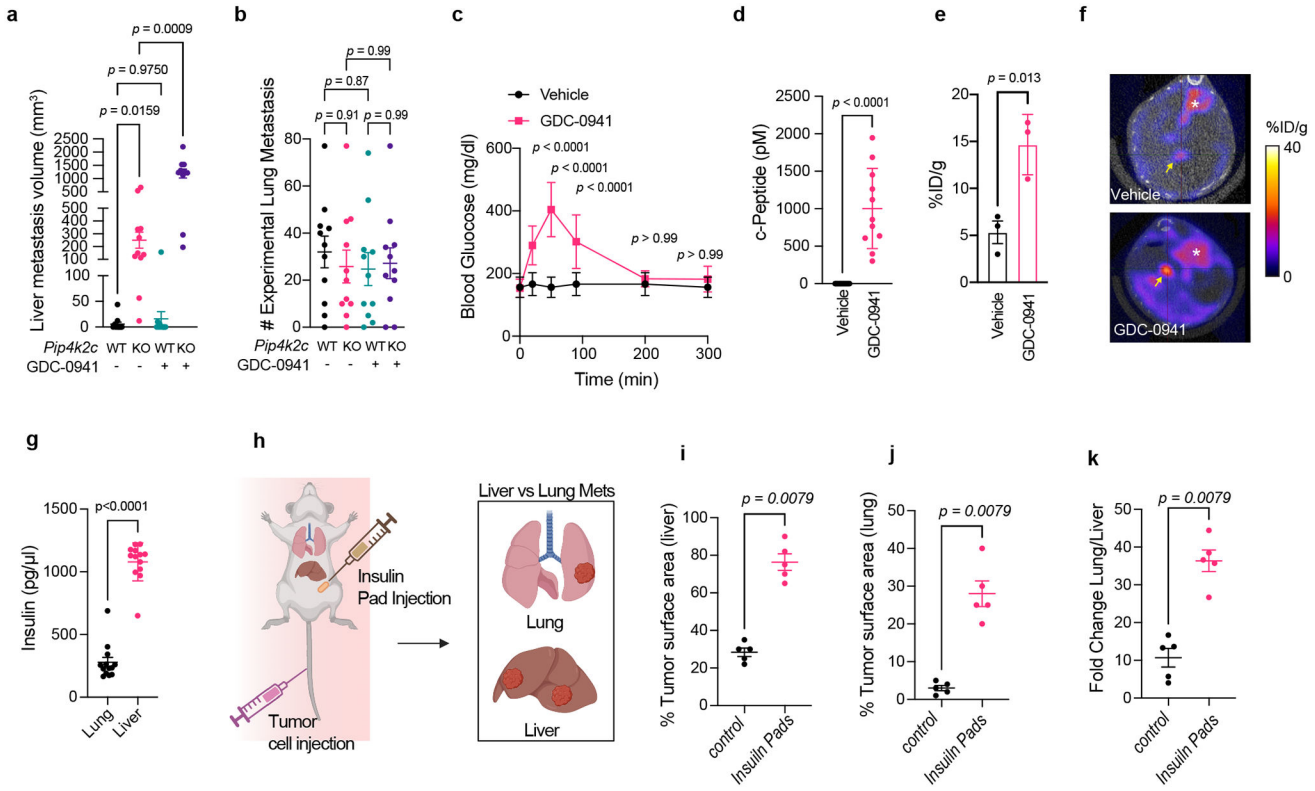

Figure 5. Genetic, dietary or pharmacological strategies disrupting systemic host effects of PI3K-inhibition reduces metastatic liver organotropism.

a, Immunoblot probing Insr in *Pip4k2c*^{KO}/*Insr*^{shIR} cells prior to use for *in vivo* experiments (in b-c). **b**, Liver metastasis disease burden (in mm^3) following tail vein injection of *Pip4k2c*^{KO}/*Insr*^{shIR} without dox, GDC-0941 alone, dox-induced *Insr* knockdown alone, and combination of dox-induced *Insr* knockdown and GDC-0941. **c**, Lung metastasis burden (metastasis count) in corresponding animals from (b); n=10 mice per group. **d**, Blood glucose levels (in mg/dL) measured in mice (n=7 mice per group) following treatment with indicated diet or drugs (30 minutes post-administration) or vehicle control. **e**, C-peptide levels (in pM) following treatment with indicated combinations of GDC-0941 with SGLT2 inhibition or animals fed with ketogenic diet (n=11 mice per group). **f**, Liver metastasis disease burden (in mm^3) following tail vein injection of *Pip4k2c*^{KO} cells with drug treatments (SGLT2i, GDC-0941), ketogenic diet or combinations thereof in indicated groups. **g**, Lung metastasis burden (metastasis count) in corresponding animals from (f); n=10 mice per group, mean± s.e.m.; **h,** Tumor growth of subcutaneously injected HCmel12 parental or *Pip4k2c* KO melanoma cell lines following no treatment, treatment with GDC-0941 alone, or combination of GDC-0941 plus SGLT2 inhibition; n=5 mice per group, mean± s.e.m. **i**, Tumor diameter at day 24 in indicated treatment and genotype groups from (h). Box plots denote the minima, maxima and median in (h). Statistical significance was determined using One-Way ANOVA Tukey's multiple comparisons test for (b-h). Data are representative of three (b-g) and two (h, i) independent experiments. Significance levels as indicated.

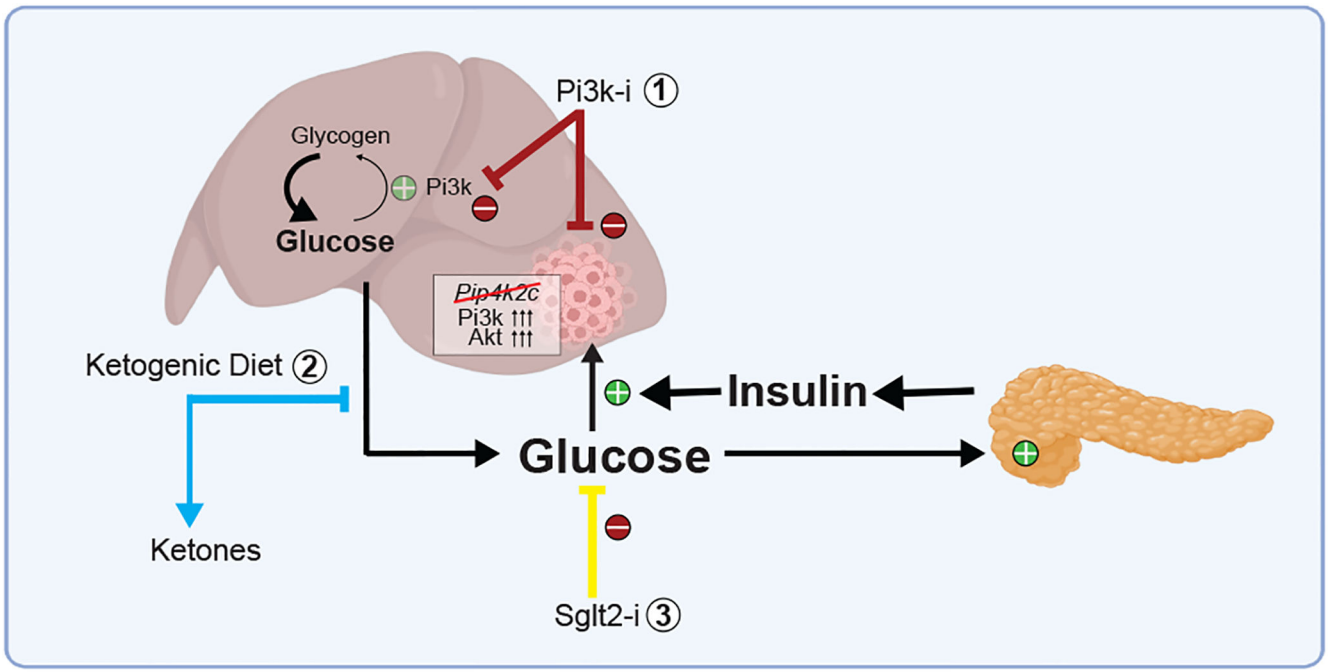

Figure 6. Schematic of Liver metastatic organotropism.

Model illustrating increased liver metastatic burden in animals injected with *Pip4k2c*^{KO} cells, (1) effects of systemic PI3K inhibition, and strategies to overcome compensatory feedback loop and increased liver metastatic burden with either (2) ketogenic diet or (3) SGLT2-inhibition.